

## Article

# MHD Natural Convection and Radiation over a Flame in a Partially Heated Semicircular Cavity Filled with a Nanofluid

Obai Younis <sup>1,2,\*</sup>, Milad Alizadeh <sup>3</sup>, Ahmed Kadhim Hussein <sup>4</sup> , Bagh Ali <sup>5</sup> , Uddhaba Biswal <sup>6</sup>  
and Emad Hasani Malekshah <sup>7</sup> 

- <sup>1</sup> Department of Mechanical Engineering, College of Engineering at Wadi Addwaser, Prince Sattam Bin Abdulaziz University, Wadi Addwaser 11991, Saudi Arabia
- <sup>2</sup> Department of Mechanical Engineering, Faculty of Engineering, University of Khartoum, Khartoum 11111, Sudan
- <sup>3</sup> Department of Thermofluid, Faculty of Mechanical Engineering, Babol Nooshirvani University of Technology, Babol 47148-71167, Iran; milad\_alizadeh\_kntu@yahoo.com
- <sup>4</sup> Mechanical Engineering Department, College of Engineering, University of Babylon, Hilla 00964, Iraq; ahmedkadhim7474@gmail.com
- <sup>5</sup> Faculty of Computer Science and Information Technology, Superior University, Lahore 54000, Pakistan; baghalisewag@mail.nwpu.edu.cn
- <sup>6</sup> Department of Mathematics, National Institute of Technology Rourkela, Rourkela 769008, India; uddhababiswal789@gmail.com
- <sup>7</sup> Department of Power Engineering and Turbomachinery, Silesian University of Technology, 44-100 Gliwice, Poland; emad.hasani@polsl.pl
- \* Correspondence: o.elamin@psau.edu.sa



**Citation:** Younis, O.; Alizadeh, M.; Kadhim Hussein, A.; Ali, B.; Biswal, U.; Hasani Malekshah, E. MHD Natural Convection and Radiation over a Flame in a Partially Heated Semicircular Cavity Filled with a Nanofluid. *Mathematics* **2022**, *10*, 1347. <https://doi.org/10.3390/math10081347>

Academic Editor: Efstratios Tzirtzilakis

Received: 7 March 2022

Accepted: 12 April 2022

Published: 18 April 2022

**Publisher's Note:** MDPI stays neutral with regard to jurisdictional claims in published maps and institutional affiliations.



**Copyright:** © 2022 by the authors. Licensee MDPI, Basel, Switzerland. This article is an open access article distributed under the terms and conditions of the Creative Commons Attribution (CC BY) license (<https://creativecommons.org/licenses/by/4.0/>).

**Abstract:** The numerical analysis of MHD-free convective heat transfer and its interaction with the radiation over a heated flame inside a porous semicircular cavity loaded with SWCNTs–water nanofluid was explored for the very first time in the present work. The two circular arcs of the upper wall of the enclosure were preserved at a constant cold temperature, whereas the middle region of it was considered adiabatic. The midland region of the lower wall was heated partially, while other regions were also assumed adiabatic. An internal hot flame was included inside the cavity, while the cavity was exposed to a magnetic field. The results were illustrated for Hartmann number ( $0 \leq Ha \leq 100$ ), Rayleigh number ( $10^4 \leq Ra \leq 10^6$ ), heated region length ( $0.1 \leq L \leq 0.3$ ), solid volumetric fraction ( $0 \leq \phi \leq 0.04$ ), Darcy number ( $10^{-3} \leq Da \leq 10^{-5}$ ) and radiation parameter ( $0 \leq Rd \leq 1$ ). It was found that decreasing L is the best option for enhancing natural convection. Moreover, it was noted that ( $Nu_{out}$ ) is directly proportion to (Ra), ( $\phi$ ), (Rd) and (Da) increase. In contrast, it was in reverse proportion to (Ha). Furthermore, the results showed that augmentation of about (4%) and a decrement of (56.55%) are obtained on the average (Nu) on the heated length by increasing the radiation and the Hartmann number, respectively. Moreover, raising the radiation number from (0 to 1) causes an augmentation of about (73%) in the average (Nu) of the heated flame. Results also indicated that increasing the Hartmann number will cause a decrement of about (82.4%) of the maximum velocity profile in the vertical direction.

**Keywords:** nanofluid; natural convection; magneto-hydrodynamic; porous media; semicircular enclosure; radiation; flame

**MSC:** 35Q30; 76M10; 80M10

## 1. Introduction

Nanotechnology is a recent science which appeared after the invention of a new kind of fluid which was termed by Choi [1] in 1995 as nanofluid. Nanoparticles include metal or non-metal oxides and metallic or non-metallic, while ethylene glycol, water and mineral oil are examples of the base fluid [2,3]. The nanofluid was entered rapidly and

strongly in many practical fields such as the biomedical industry, solar energy systems, air-conditioning and refrigeration, heat exchangers and car radiators [4]. The reader can find very intense information about the nanofluid in many review papers like Sajid and Ali [5], Kamel et al. [6] and Pordanjani et al. [7]. On the other side, buoyancy-driven convection, usually termed the natural convection in enclosures loaded with a nanofluid, is a very interesting phenomenon investigated by many researchers [8–12]. Of course, the major reason behind this attention is due to its very wide applications in many engineering fields. Examples of these applications include heat exchangers, cooling of flush-mounted electronic heaters and the building industry [13].

On the other hand, the magnetic field can play an important role in controlling the free convection of nanofluids flow inside enclosures. The mixed effects of the natural convection and the magnetic field are called magnetohydrodynamic (MHD) convection [14]. This subject has efficiently been applied in the polymer industry, fusion reactors, electronic packages, crystal growth in liquids, and geothermal energy extraction [15–17].

Natural convection in enclosures with intricate geometry, loaded with a nanofluid, and exposed to a magnetic field has recently attracted the attention of researchers. This is owing to the fact that it has a wide range of uses in industrial and engineering applications. Several of these applications are illustrated via packed bed reactors of solar systems, petroleum resources, ventilation of buildings, and purification of molten metals, liquid metals and microelectronic devices [18]. Various researchers explored the natural convection in irregular enclosures loaded with nanofluid in the existence of the magnetic field. The influence of the vertical magnetic field on the free convection inside a triangular cavity loaded with Cu–water nanofluid was performed numerically by Mahmoudi et al. [19]. The tilted right side of the cavity was preserved at a cold temperature, whereas the bottom wall was thought to be partially heated. The left vertical wall, together with the remaining regions in the bottom wall, were assumed thermally insulated. The impacts of the  $Ha$  ( $0 \leq Ha \leq 100$ ), solid volume fraction ( $0 \leq \phi \leq 0.05$ ), Rayleigh number ( $10^4 \leq Ra \leq 10^7$ ) together with six different cases of the heat source location on the  $(Nu_{av})$  Streamline, and isotherm were examined. A distinct depression in the flow field and heat transfer for high  $(Ha)$  was noted. Sheikholeslami et al. [20] employed the control volume finite element technique to explore the magnetohydrodynamic natural convection in a tilted half-annulus enclosure loaded with copper-water nanofluid. The findings were reported for a range of inclination angle values  $(Ha)$ , solid volume fraction and  $(Ra)$ . It was noted that the  $(Nu_{av})$  was augmented by raising the solid volume fraction and  $(Ra)$  and decreasing  $(Ha)$ . The MHD free convection in a tilted trapezoidal cavity loaded with Cu–water nanofluid was numerically carried out by Mansour et al. [21]. The results were illustrated for various values of the  $(Ha)$ , enclosure inclination angle,  $(Ra)$ , heat source length and its location and the solid volume fraction. They demonstrated that the maximum heat transfer rate was observed at  $(Ha = 0$  and  $Ra = 10^6)$ . The natural convection problem inside a semi-annulus enclosure loaded with alumina-water nanofluid under the impact of the magnetic field was solved numerically by Sheikholeslami et al. [22]. The results were illustrated for Hartmann number ( $0 \leq Ha \leq 100$ ), a solid volume fraction ( $0 \leq \phi \leq 0.04$ ) and Rayleigh number ( $10^4 \leq Ra \leq 10^6$ ). They concluded that  $(Nu_{av})$  was decreased with increasing  $(Ha)$ , while a reverse trend was noted with increasing  $(Ra)$  and the solid volume fraction. Aminossadati [23] numerically explored the MHD natural convection inside a triangular enclosure loaded with CuO–water nanofluid. The cavity included inside it a right triangular heat source. He deduced that the maximum heat transfer rate was found at high values of the solid volume fraction and  $(Ra)$ . Whereas it was reduced by magnifying the magnetic field strength. The numerical analysis of the free convection of Cu–water nanofluid in a tilted, differentially heated L-shaped cavity with the existence of the magnetic field was researched by Elshehabey et al. [24]. It was deduced that  $(Nu_{av})$  was increased by decreasing the aspect ratio or  $(Ha)$ . It decreased by decreasing  $(Ra)$  or the solid volume fraction. Al-Zamily [25] explored the magnetic field effect on the free convection within a semicircular cavity loaded with Cu–water nanofluid by numerical means. He deduced that the magnetic

field's impact on the natural convective flow was retreated by increasing the solid volume fraction. Whereas it increased by increasing (Ra). Sheikholeslami et al. [26] employed numerical methods to examine the magnetic field influence on a wavy cavity loaded with CuO–water nanofluid. The results were displayed for a broad variety of (Ra) and (Ha) numbers, the dimensionless amplitude of the sinusoidal wall and the solid volume fraction. It was noticed that ( $Nu_{av}$ ) was augmented by raising the solid volume fraction, (Ra) and sinusoidal wall amplitude. While it damped by increasing (Ha). Sheikholeslami et al. [27] examined numerically the free convection in a tilted L-shaped cavity loaded with alumina–water nanofluid and exposed to the magnetic field. Their findings were shown for various values of the solid volume fraction, inclination angle, (Ha) and (Ra) numbers. The authors determined that the greatest heat transfer increase was obtained at high (Ha) and low (Ra). The impact of the tilted magnetic field on the transient free convection inside a right-angle trapezoidal cavity was performed numerically by Bondareva et al. [28]. The impacts of the magnetic field inclination angle, dimensionless time, aspect ratio and Lewis, (Ha) and (Ra) numbers on the flow and thermal fields were examined. They concluded that the Sherwood and Nusselt numbers were enhanced by increasing the magnetic field inclination angle and (Ra). Hussein et al. [29] numerically explored the magnetic field effect on a tilted T-geometry cavity loaded with various types of nanofluid. It was found that ( $Nu_{av}$ ) was increased with the solid volume fraction as the heat source location increased and its length decreased. Yadollahi et al. [30] numerically analysed the MHD natural convection within an F-geometry cavity loaded with sliver-water nanofluid. The influence of the aspect ratio, (Ra) and (Ha) numbers were considered. It was noted that the impact of the magnetic field strength on ( $Nu_{av}$ ) was increased by increasing (Ra). Ali et al. [31] performed the magneto-hydrodynamic free convection in a hexagonal cavity with a tilted block numerically. The cavity was loaded with CuO–water nanofluid. It was concluded that ( $Nu_{av}$ ) was decreased by decreasing (Ra) and the solid volume fraction and increasing the magnetic field strength. Purusothaman and Malekshah [32] numerically examined the MHD natural convection inside a tilted V-shaped cavity loaded with Cu–water nanofluid. The influence of (Ha) and (Ra) numbers, solid volume fraction and the cavity tilting angle and its aspect ratio on the fluid and heat flow structures in the cavity were considered. It was deduced that ( $Nu_{av}$ ) was reduced by decreasing (Ra) and the solid volume fraction. It was increased by decreasing (Ha) the aspect ratio. Ghani et al. [33] explored the MHD free convection inside a parallelogrammic cavity loaded with Cu–water nanofluid by numerical means. The right sidewall of it was assumed open to the environment, while the left one was subjected to a localised heat source. Both the top and bottom tilted walls were maintained cold. The effects of Ra ( $10^4 \leq Ra \leq 10^6$ ), inclination angle ( $-60^\circ \leq \lambda \leq 60^\circ$ ), heat source location ( $0.25 \leq \varepsilon \leq 0.75$ ), solid volume fraction ( $0 \leq \phi \leq 0.04$ ) and Ha ( $0 \leq Ha \leq 75$ ) on the flow, thermal fields and ( $Nu_{av}$ ) were examined. The heat source length was kept fixed at ( $\delta = 0.25$ ). It was noted that ( $Nu_{av}$ ) was increased with increasing (Ra) and decreasing (Ha), and its value for nanofluid was more than that for water. The impact of the inclined magnetic field on the free convection inside a trapezoidal enclosure loaded with alumina–water nanofluid was addressed by Saha [34]. He deduced that the flow and thermal fields became weak by increasing the aspect ratio. Moreover, the solid volume fraction increment slightly influenced the heat transfer rate. Other useful references deal with heat transfer within complex shaped geometries loaded with the nanofluid can be found in [35–41].

On the other hand, the free convection inside enclosures loaded with a porous medium has been considered one of the most significant research subjects due to its numerous practical applications such as domestic heating, polymer processing, and energy extraction [42–45]. Al-Hafidh and Mohammed [46] numerically examined the free convection of Cu–water nanofluid inside a cylindrical enclosure loaded with a porous media. They presented their research findings for a wide range of (Ra), aspect ratio (A) and solid volume fraction. It was found that ( $Nu_{av}$ ) was enhanced by increasing both (Ra) and (A). Mansour et al. [47] numerically researched the natural convection inside an H-shaped enclosure loaded with various nanofluids saturated with a porous media. Various nanopar-

ticles were utilised (i.e., Ag, Cu, TiO<sub>2</sub> and Al<sub>2</sub>O<sub>3</sub>). The thermal and flow fields characteristics were presented for Rayleigh number ( $50 \leq Ra \leq 1000$ ), solid volume fraction ( $0 \leq \varphi \leq 0.1$ ), heat source length ( $0.2 \leq B \leq 0.8$ ), aspect ratio ( $0.2 \leq AR \leq 0.8$ ) and heat source location ( $0.2 \leq D \leq 0.5$ ). The results indicated that ( $Nu_{av}$ ) was decreased with increasing the solid volume fraction and heat source length. The free convection in a tilted hemispherical enclosure loaded with Cu–water nanofluid saturated with a porous media was numerically researched by Bairy et al. [48]. The authors were able to propose a correlation to calculate the average temperature of the active dome of enclosure in terms of ( $Ra$ ), solid volume fraction, tilting angle and the thermal conductivity ratio. The free convection inside an E-enclosure loaded with Al<sub>2</sub>O<sub>3</sub>-water nanofluid was explored by Raizah et al. [49]. The findings were presented for a wide range of ( $Da$ ), ( $Ra$ ), solid volume fractions and six cases of the porous media. They concluded that ( $Nu_{av}$ ) was maximum for horizontal heterogeneous porous media. The numerical analysis of MHD free convection in a novel-shaped cavity was researched by Molana et al. [50]. The cavity was loaded with Fe<sub>3</sub>O<sub>4</sub>-water nanofluid and saturated with a porous medium. The analysis was performed for various values of ( $Ha$ ), ( $Ra$ ), ( $Da$ ) and ( $AR$ ) and cavity inclination angle. The results referred that ( $Nu_{av}$ ) was enhanced by increasing ( $Ra$ ) and ( $AR$ ).

The combination of the free convection and radiation inside enclosures has various technological applications like transpiration cooling process, high temperatures energy conversion systems and cover material drying [51]. The numerical study of the radiation impact on the MHD free convection inside a semi-annulus enclosure loaded with iron oxide-water nanofluid was performed by Sheikholeslami et al. [52]. The authors observed that ( $Nu_{av}$ ) was increased by decreasing ( $Rd$ ) and ( $Ha$ ). At the same time, it was increased by increasing ( $Ra$ ) and solid volume fraction. The mixed impacts of the magnetic field and radiation on the free convection and entropy production in a tilted square enclosure included a circular baffle loaded with alumina–water nanofluid was numerically researched by Li et al. [53]. The research findings were shown for various values of cavity inclination angle ( $Rd$ ), the solid volume fraction ( $Ha$ ), ( $Ra$ ) and baffle aspect ratio. The authors concluded that the free convection was augmented by increasing the radiation and existence of the nanofluid.

Based on the above literature review, and in spite of a large number of published papers on natural convection, the MHD natural convection and its interaction with the radiation over a heated flame inside a partially heated porous semicircular cavity filled with SWCNTs–water nanofluid were not studied previously in any paper. Moreover, the SWCNT nanoparticles with various solid volume fractions were dispersed in the water to enhance their thermal conductivity. Moreover, a parametric study has been done to investigate the effect of the magnetic field, porosity, radiation, Rayleigh number and heated length on the heat transfer and flow field inside the semicircular cavity. These points can be considered novelties of the current work.

## 2. Geometrical Configuration and the Governing Equations

Figures 1 and 2 show the schematic diagram and mesh distribution of a 2D semicircular cavity, respectively. The two circular arcs of the upper cavity wall were preserved at a constant cold temperature ( $T_c$ ), whereas the middle region of it was considered adiabatic. The midland region of the lower wall was heated partially, while other regions were assumed adiabatic also. The cavity was loaded with SWCNTs–water nanofluid. An internal hot flame was included inside the cavity while the cavity was subjected to a magnetic field. The thermophysical characteristics of the nanoparticles are presented in Table 1. The governing equations that capture the physics of this problem are introduced in Section 3. This section implemented a discretisation method to discretise the governing equations, and a numerical scheme was developed. To this end, the Standard Galerkin Finite Element Method (SGFEM) is implemented to discretise the governing equations. FlexPDE 5.0.18 software package was utilised for numerical modelling, and triangular gridding was used for the meshing process.

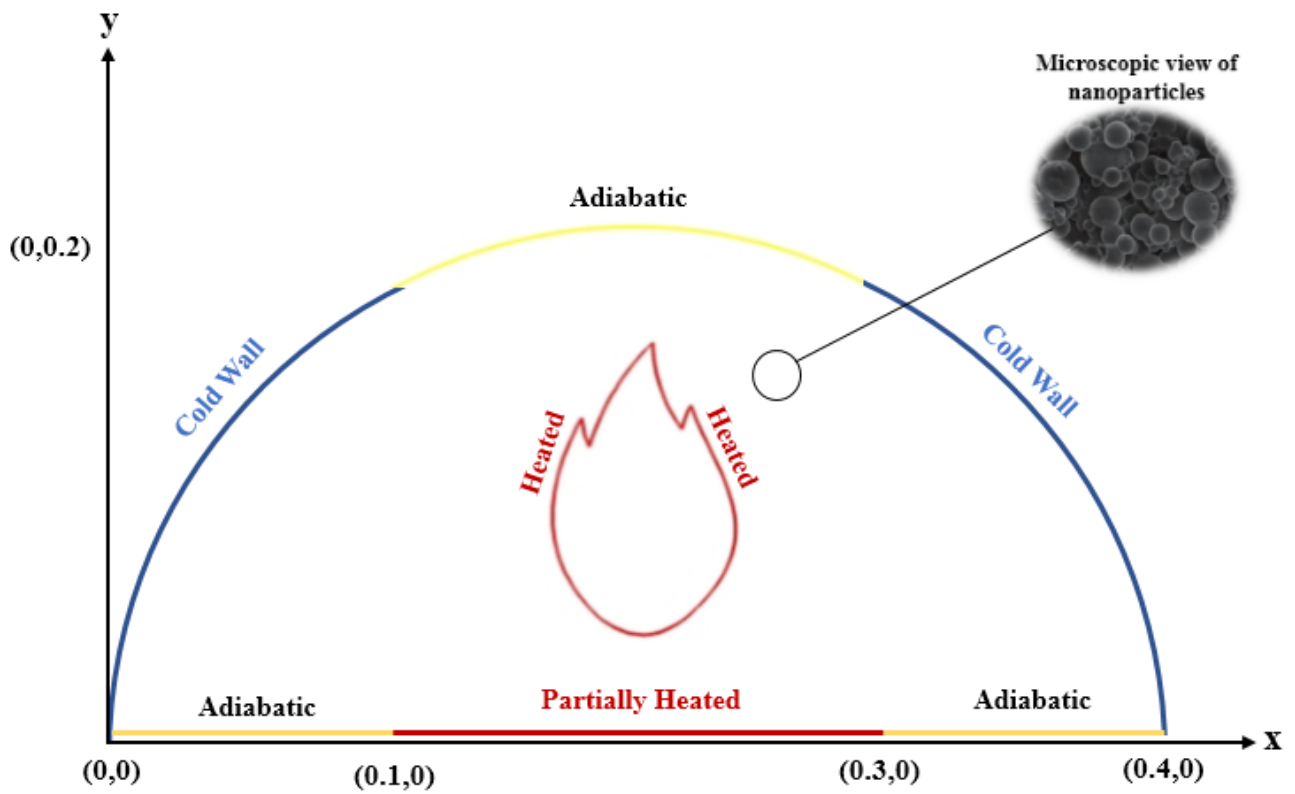


Figure 1. Schematic diagram of the present problem.

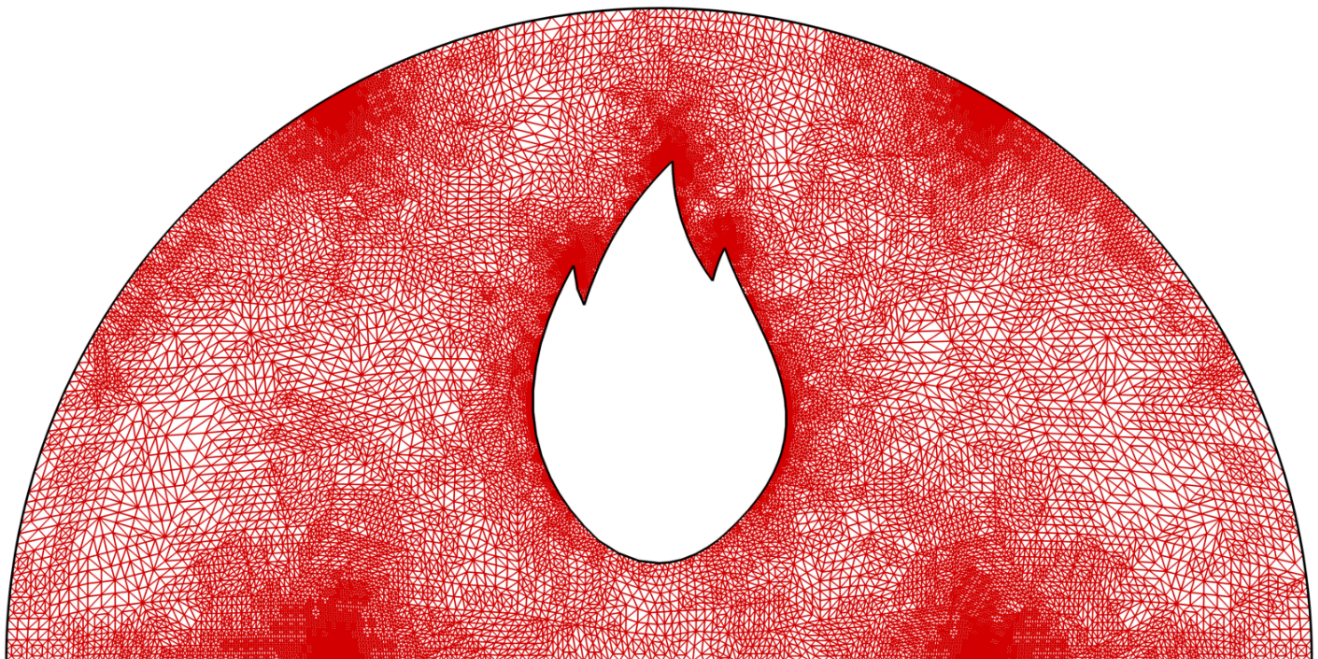
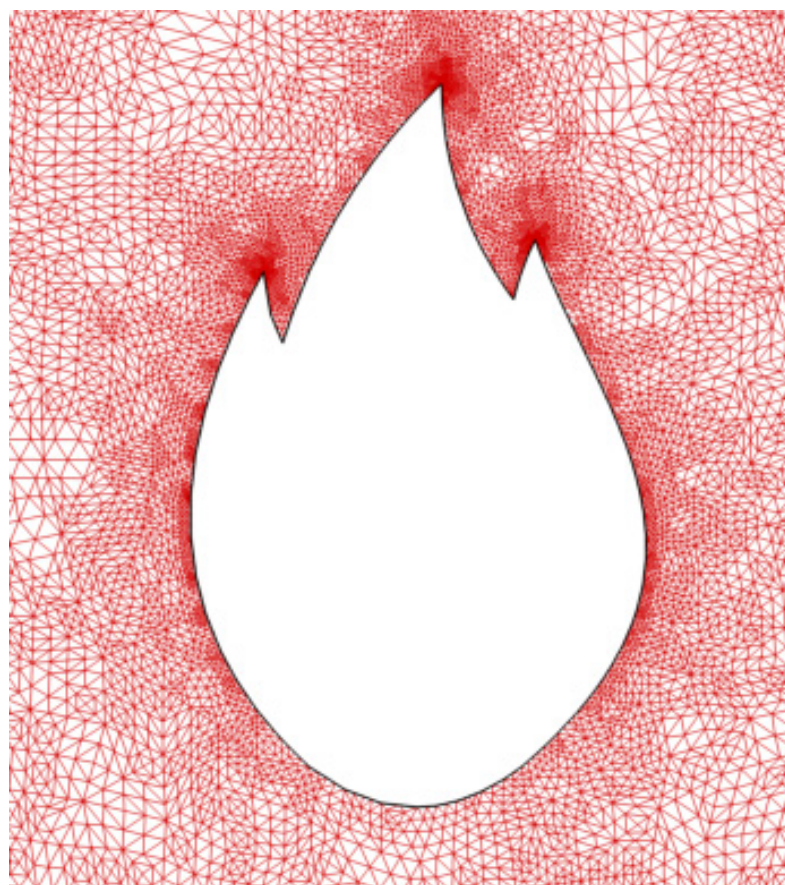


Figure 2. Cont.



**Figure 2.** Computational domain mesh distribution.

**Table 1.** Thermophysical characteristics of nanoparticles [25].

Physical Properties	Nanoparticle (SWCNT)
$c_p$ (J/kg·K)	425
$\rho$ (kg/m <sup>3</sup> )	2600
$K$ (W/mK)	6600
$\beta$ (1/K)	$0.033 \times 10^5$

To increase the accuracy of this numerical solution, a dynamic mesh adaptive technique was implemented. This method refined the grids with considerable variable alteration to capture the phenomenon accurately, as shown in Figure 2. In the adaptive grid refinement process, each cell where the error exceeds the defined error limit is subdivided until the desired accuracy is achieved. It should be noted that the defined error limit is applied either on spatial or time scales. Considering high values for error limit allows the existence of coarse mesh in the solution domain, while the accuracy will not be acceptable. Small values of error limit lead to too small mesh cells, which increases the computational cost.

An implicit backward difference method was utilised for discretisation, and the developed Galerkin matrix was solved numerically using the Newton–Raphson method. First, the accuracy of this developed numerical simulation should be verified. Therefore, the number of cells in this study is (9423), the relative error limit equals (0.0001), and an acceptable accuracy and CPU time were achieved.

On the other hand, the following assumptions were used for modelling the governing equations:

- The SWCNTs are homogeneous in shape and size and well scattered in water.

- To account for density fluctuation, the Boussinesq model was used. In comparison, the other thermo-physical properties are kept constant.
- The flow field is assumed Newtonian, laminar, 2D and steady.
- The thermal equilibrium state was assumed between the water and SWCNTs from one side and between the porous medium and SWCNTs from the other side.

### 3. Governing Equations

According to the assumptions mentioned above, the equations which govern the problem read:

$$\frac{\partial u}{\partial x} + \frac{\partial v}{\partial y} = 0 \tag{1}$$

$$\rho_{nf}(u \frac{\partial u}{\partial x} + v \frac{\partial u}{\partial y}) = -\frac{\partial p}{\partial x} + \mu_{nf}(\frac{\partial^2 u}{\partial x^2} + \frac{\partial^2 u}{\partial y^2}) - \frac{\mu_{nf}}{K}u \tag{2}$$

$$\rho_{nf}(u \frac{\partial v}{\partial x} + v \frac{\partial v}{\partial y}) = -\frac{\partial p}{\partial y} + \mu_{nf}(\frac{\partial^2 v}{\partial x^2} + \frac{\partial^2 v}{\partial y^2}) - \frac{\mu_{nf}}{K}v - \frac{\sigma}{\rho_{nf}}B_0^2v - g\rho_{nf}\beta_{nf}(T^* - T_C) \tag{3}$$

$$u \frac{\partial T^*}{\partial x} + v \frac{\partial T^*}{\partial y} = \alpha_{nf}(\frac{\partial^2 T^*}{\partial x^2} + \frac{\partial^2 T^*}{\partial y^2}) - (\frac{1}{(\rho C_p)_{nf}}) \frac{\partial q_r}{\partial y}, \tag{4}$$

where,  $q_r = -(4 \frac{\sigma_r}{\chi_r}) \frac{\partial T^4}{\partial y}$ ,  $T^4 \cong -3T_C^4 + 4T_C^3T$

In these equations,  $u$  and  $v$  denote velocity components along  $x$  and  $y$  directions. The thermophysical properties of the nanofluid, including the density, viscosity, coefficient of thermal expansion and thermal diffusivity, are presented as  $\rho_{nf}$ ,  $\mu_{nf}$ ,  $\beta_{nf}$  and  $\alpha_{nf}$ .  $T^*$  illustrates the temperature, and  $p$  shows the pressure.

In addition, the thermophysical characteristics of the nanofluid read [17]:

$$\left\{ \begin{array}{l} \beta_{nf} = (1 - \phi)\beta_f + \phi\beta_p, \\ \rho_{nf} = (1 - \phi)\rho_f + \phi\rho_p, \\ (\rho C_p)_{nf} = (1 - \phi)(\rho C_p)_f + \phi(\rho C_p)_p, \\ \alpha_{nf} = \frac{k_{nf}}{(\rho C_p)_{nf}}, \\ \frac{k_{nf}}{k_f} = \frac{(1 - \phi) + 2\phi(\frac{k_p}{k_p - k_f}) \ln(\frac{k_p - k_f}{2k_f})}{(1 - \phi) + 2\phi(\frac{k_f}{k_p - k_f}) \ln(\frac{k_p + k_f}{2k_f})}, \\ \frac{\mu_{nf}}{\mu_f} = \frac{1}{(1 - \phi)^{2.5}}, \end{array} \right. \tag{5}$$

where  $\beta_f$ ,  $\beta_p$ ,  $\rho_f$ ,  $\rho_p$ ,  $(C_p)_f$ ,  $(C_p)_p$ ,  $k_f$  and  $k_p$  are the coefficient of thermal expansion, density, particular heat capacity, and thermal conductivity of the base fluid and nanoparticles each. Moreover,  $\mu_f$  demonstrates the dynamic viscosity of the base fluid;  $\phi$  shows the volumetric fraction of the nanoparticles. The following boundary conditions have been applied:

Along the outer walls:

At the side arcs walls:

$$T^* = T_C \tag{6}$$

At the bottom walls:

$$\begin{aligned} \frac{\partial T^*}{\partial y} &= 0, \text{ Adiabatic sidewalls} \\ T^* &= T_h, \text{ Partially heated central wall} \end{aligned} \tag{7}$$

For the top central arc wall:

$$\frac{\partial T^*}{\partial y} = 0 \tag{8}$$

On all walls:

$$u = v = 0 \tag{9}$$

Along the inner walls:

$$T^* = T_h \tag{10}$$

The following dimensionless variables are applied to the governing equations:

$$\begin{aligned} X &= \frac{x}{L}, Y = \frac{y}{L}, U = \frac{uL}{\alpha_f}, V = \frac{vL}{\alpha_f}, T = \frac{T^* - T_C}{T_h - T_C}, P = \frac{pL^2}{\rho_f \alpha_f^2}, \vartheta_f = \frac{\mu_f}{\rho_f}, \text{Pr} = \frac{\vartheta_f}{\alpha_f}, \\ \text{Ha} &= B_0 L \sqrt{\frac{\sigma}{\rho_{nf} \vartheta_f}}, \text{Rd} = \frac{4\sigma_r T_C^3}{\chi_r k_f}, P = -\gamma \left( \frac{\partial U}{\partial X} + \frac{\partial V}{\partial Y} \right), \\ \text{Ra} &= \frac{\beta_f (T_h - T_C) L^3}{\vartheta_f \alpha_f}. \end{aligned} \tag{11}$$

here, Pr, Ra, Ha and Rd show the Prandtl number, Ra, Ha and radiation parameter.  $\gamma$  is assumed to be equal to  $10^7$  to eliminate the pressure from the momentum equations. Using these parameters, the dimensionless forms of the governing equations read [42]:

$$\frac{\partial U}{\partial X} + \frac{\partial V}{\partial Y} = 0 \tag{12}$$

$$U \frac{\partial U}{\partial X} + V \frac{\partial U}{\partial Y} = \gamma \frac{\rho_f}{\rho_{nf}} \frac{\partial}{\partial X} \left( \frac{\partial U}{\partial X} + \frac{\partial V}{\partial Y} \right) + \text{Pr} \frac{\vartheta_{nf}}{\vartheta_f} \left( \frac{\partial^2 U}{\partial X^2} + \frac{\partial^2 U}{\partial Y^2} \right) - \frac{\text{Pr}}{\text{Da}} U, \tag{13}$$

$$\begin{aligned} (U \frac{\partial V}{\partial X} + V \frac{\partial V}{\partial Y}) &= \gamma \frac{\rho_f}{\rho_{nf}} \frac{\partial}{\partial Y} \left( \frac{\partial U}{\partial X} + \frac{\partial V}{\partial Y} \right) + \text{Pr} \frac{\vartheta_{nf}}{\vartheta_f} \left( \frac{\partial^2 V}{\partial X^2} + \frac{\partial^2 V}{\partial Y^2} \right) - \text{Ha}^2 \text{Pr} V \\ &+ \frac{(1-\phi)\rho_f\beta_f + \phi\rho_p\beta_p}{\rho_{nf}\beta_{nf}} \text{RaPr} T - \frac{\text{Pr}}{\text{Da}} V, \end{aligned} \tag{14}$$

$$U \frac{\partial T}{\partial X} + V \frac{\partial T}{\partial Y} = \frac{\alpha_{nf}}{\alpha_f} \left( \frac{\partial^2 T}{\partial X^2} + \frac{\partial^2 T}{\partial Y^2} \right) + \frac{4}{3} \text{Rd} \frac{(\rho C_p)_f}{(\rho C_p)_{nf}} \frac{\partial^2 T}{\partial Y^2}, \tag{15}$$

The non-dimensional boundary conditions read:

At the side arcs walls:

$$T = 0 \tag{16}$$

At the bottom walls:

$$\begin{aligned} \frac{\partial T}{\partial Y} &= 0, \text{ Adiabatic sidewalls} \\ T &= 1, \text{ Partially heated central wall} \end{aligned} \tag{17}$$

At the top central arc wall:

$$\frac{\partial T}{\partial Y} = 0 \tag{18}$$

Along the inner walls:

At all inner flame-shaped walls:

$$T = 1 \tag{19}$$

For all walls:

$$U = V = 0 \tag{20}$$

In addition, the average (Nu) along the partially heated wall is described as:

$$\text{Nu}_{ave} = \int_{L_T} \left( 1 + \frac{4}{3} \frac{k_f}{k_{nf}} \text{Rd} \right) \left( \frac{k_{nf}}{k_f} \right) \frac{\partial T}{\partial n} dX, \tag{21}$$

Here  $n$  represents the normal direction at the heated wall of the enclosure ( $L_T$ ).

#### 4. Numerical Procedure and Validation

In the present work, the Standard Galerkin Finite Element Method (SGFEM) is employed to lay out the fluid flow and heat transfer. With respect to its advantages, the main point is that it can be used efficiently to deal with complex geometries with an accurate and short computational time. Moreover, this method has good stability when it deals

with partial differential equations compared with conventional methods. The calculation of problems dealing with the triangle grids is accomplished on the nodes. According to this approach, differential equations are shaped by substituting the definitions, applying the dependencies on the variables, integrating over cells, and differentiating the variables of the system. The Galerkin matrix is figured through these equations. The grid refinement is performed using an adaptive technique wherever the gradient of the variables is remarkable. The grid refinement proceeds until achieving the desired precision, which is defined. To accredit the procedure, the current simulation is compared with the previously published paper by Haq et al. [54], which is presented in Figure 3 (As shown, the  $v$  profile for  $Ra = 10^5$ ,  $\phi = 0$  is plotted along the  $y$ -direction in both studies). It can be observed that an excellent agreement with the maximum error of 5% is achieved, which demonstrates the accuracy of the model. Moreover, the solution flow diagram of the current study is shown in Figure 4.

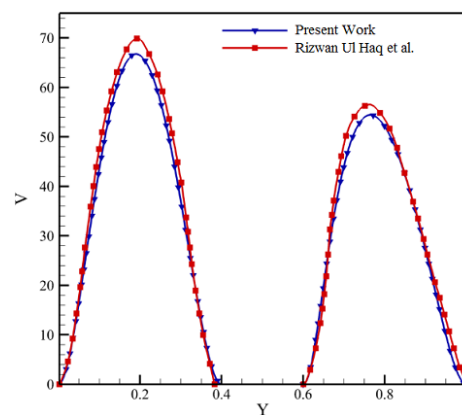


**Figure 3.** The V-velocity profile along the Y-direction at ( $\phi = 0$ ,  $Ra = 10^5$  and  $L = 0.4$ ) obtained by the present work and the results of Haq et al. [54].

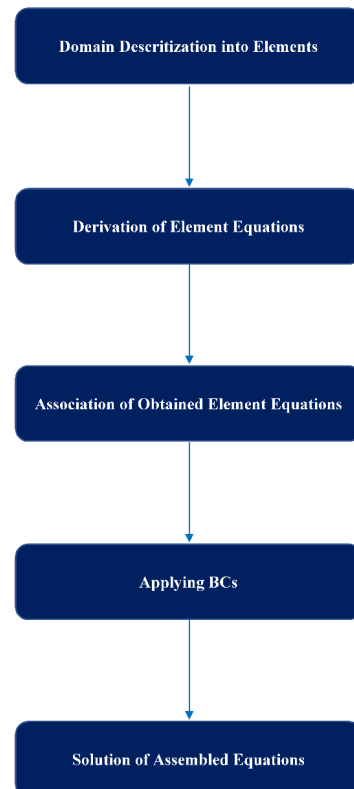


**Figure 4.** Flow diagram of the numerical solution.

## 5. Results and Discussion

The current work numerically explored the MHD free convection and its interaction with radiation over a heated flame inside a partially heated porous semicircular enclosure loaded with SWCNTs–water nanofluid. The ranges of studied controlling parameters were:  $Ha$  ( $0 \leq Ha \leq 100$ ),  $Ra$  ( $10^4 \leq Ra \leq 10^6$ ), heated region length ( $0.1 \leq L \leq 0.3$ ), solid volumetric fraction ( $0 \leq \phi \leq 0.04$ ),  $Da$  ( $10^{-3} \leq Da \leq 10^{-5}$ ), and radiation parameter ( $0 \leq Rd \leq 1$ ).

### 5.1. Effect of Rayleigh Number

The contours of streamline (right) and isotherm (left) of the nanofluid inside the semicircular cavity for various values of  $(Ra)$  at ( $\phi = 0.02$ ,  $Ha = 50$ ,  $Rd = 0.5$ ,  $Da = 10^{-4}$  and  $L = 0.2$ ) are presented in Figure 5. It may be noted that the flow field consists of two identical rotating vortices around the internal flame. The right vortices are cold, whereas the left ones are hot. The natural convection currents initiate near the hot region in the lower wall of the cavity and move upward towards the adiabatic region in the upper wall. After that, they reflect adjacent to this wall's two cold circular segments. Therefore, the nanofluid compresses and moves downward. This repetitive motion generates the cavity's two identical rotating vortices. In fact, the  $(Ra)$  is an indicator of the strength of the natural convection. The observations of Figure 4 show that the intensity of the flow circulation rises significantly with increasing  $(Ra)$ . Therefore, the peak value of the stream function jumps from ( $\psi = 0.007$ ) at ( $Ra = 10^4$ ) to ( $\psi = 0.75$ ) at ( $Ra = 10^6$ ). The cause for this tendency is due to the growth in buoyant force that occurs when the  $(Ra)$  rises. This causes the free convection to increase within the cavity. With respect to the effect of  $(Ra)$  on the flow field pattern, it can be noted that the increase in it leads to two things. The first one makes the gap between the two vortices to decrease over the internal flame. While the second thing increases the size of the internal core inside the vortices. On the other side, the increase in  $(Ra)$  leads to make changes in the isotherm contours. They become more curved, especially in the region below the internal flame. Moreover, they extend further with the increase in  $(Ra)$  toward the upper wall unit to touch at ( $Ra = 10^6$ ). This is a signal that the heat transfer mechanism shifts from conduction to convection with the increase in  $(Ra)$ .

The variation of  $(Nu_{out})$  at the heated wall of the cavity, temperature and velocity profiles alongside the mean vertical location for different values of  $(Ra)$  at ( $\phi = 0.02$ ,  $Ha = 50$ ,  $Rd = 0.5$ ,  $Da = 10^{-4}$  and  $L = 0.2$ ) are illustrated respectively in Figure 6a–c. For all values of  $(Ra)$ , it can be noted from Figure 6a that  $(Nu_{out})$  increases with the increase in it. This is a logical result due to the increase in the buoyancy force with increasing  $(Ra)$ . This leads to improving natural convection and enhances  $(Nu_{out})$  values. In addition, it can be noted from Figure 6a that  $(Nu_{out})$  drops gradually along  $(X)$  until  $(X = 0.1)$  and then starts to increase after that. The temperature and velocity profiles along the mean vertical location of the semicircular cavity for various values of  $(Ra)$  are explained respectively in Figure 6b,c. It can be noted from Figure 6b that the  $(T)$  varies approximately linear along  $(Y)$  up to  $(Y = 0.15)$  and increases with the decrease in  $(Ra)$ , as shown in the block zoom in this figure. After that, it begins to drop sharply and increases with the increase in  $(Ra)$ . For Figure 6c, it can be seen that the velocity varies slightly along  $(Y)$  until  $(Y = 0.15)$  and then begins to jump suddenly after that. This jump in  $(V)$  values begins to decrease rapidly with the decrease of  $(Ra)$  from ( $Ra = 10^6$ ) to ( $Ra = 10^4$ ).

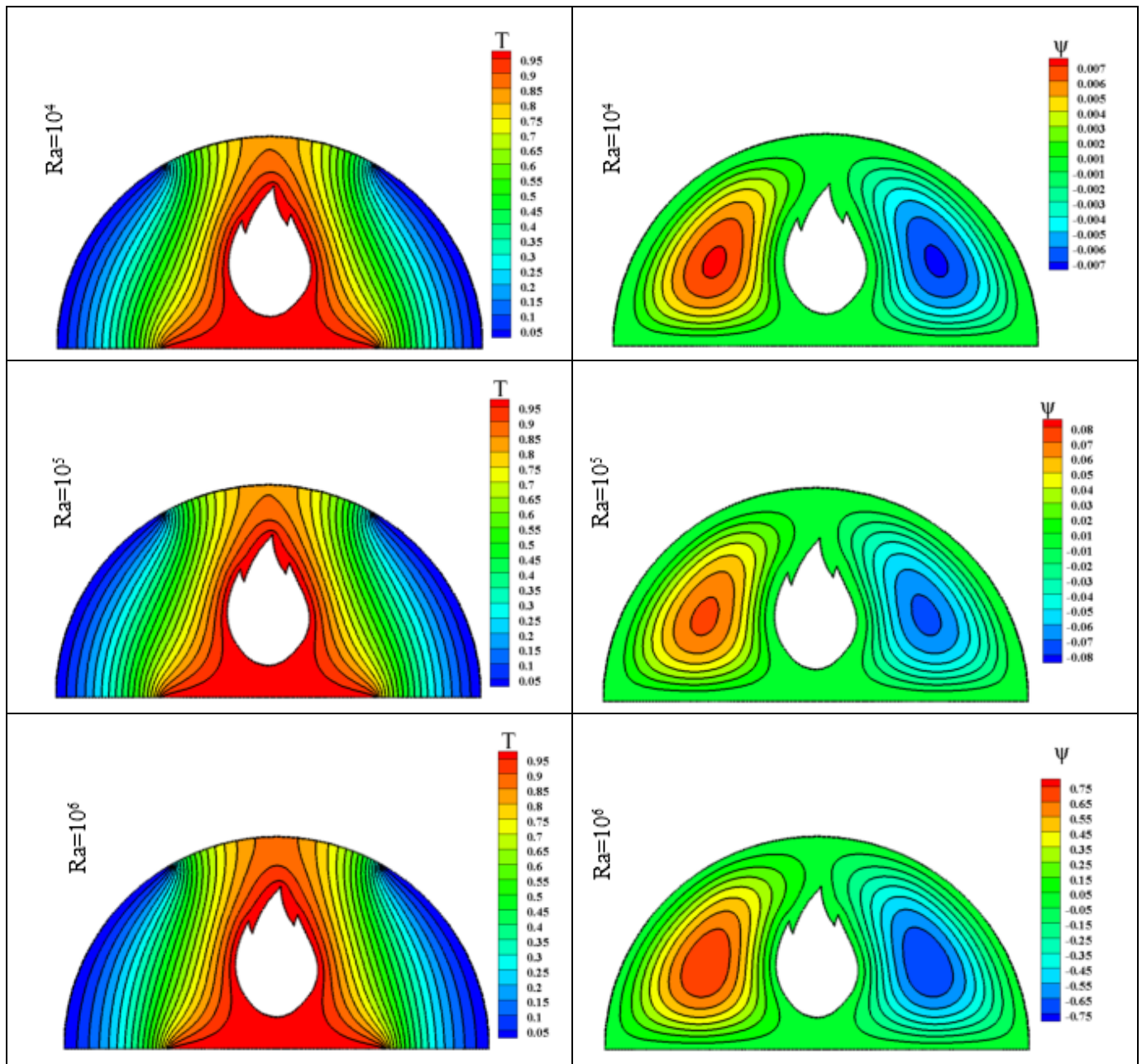
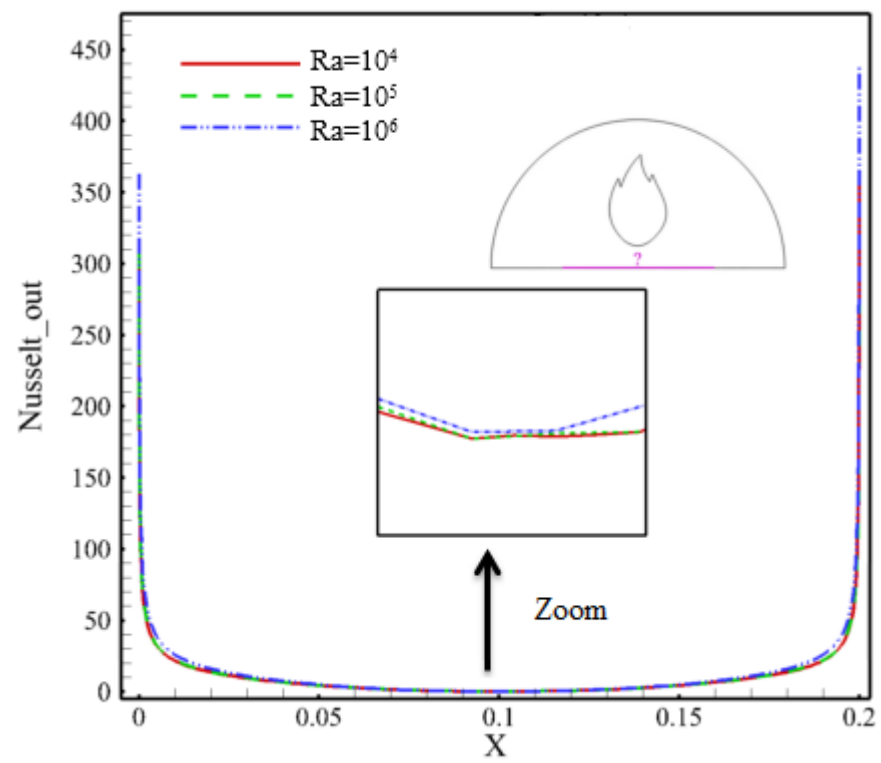
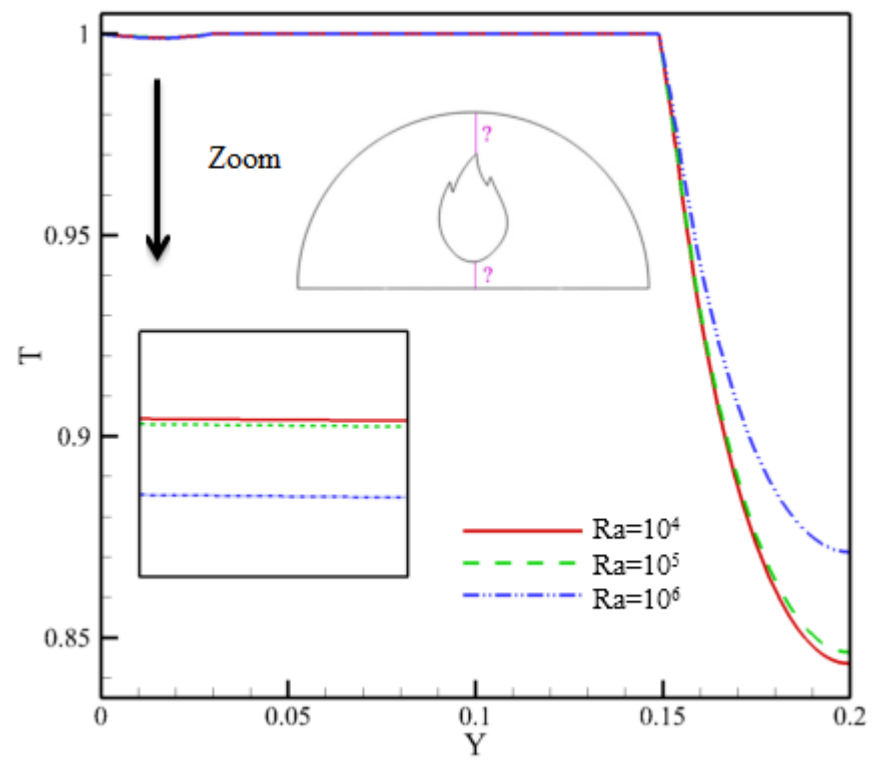


**Figure 5.** Streamlines (right) and isotherms (left) for different Ra ( $\phi = 0.02$ , Ha = 50 and Rd = 0.5, Da =  $10^{-4}$  and L = 0.2).



(a)



(b)

Figure 6. Cont.

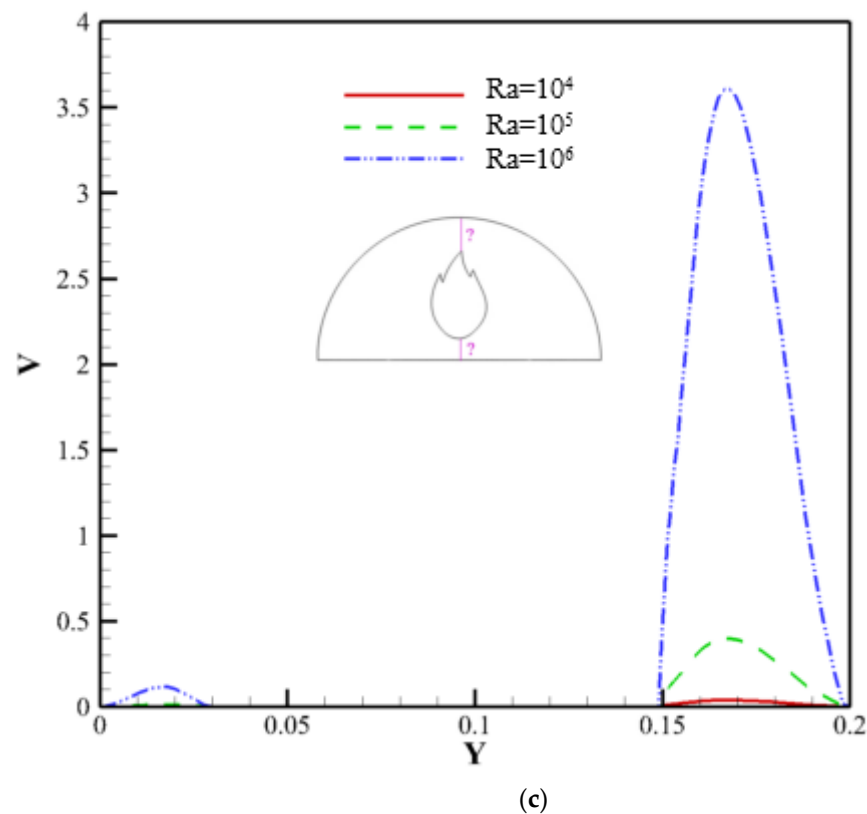


**Figure 6.** Variation of (a) Nusselt number at the enclosure heated wall, (b) temperature along vertically mean position and, (c) velocity alongside mean vertical location for different values of Ra at ( $\phi = 0.02$ ,  $Ha = 50$ ,  $Rd = 0.5$ ,  $Da = 10^{-4}$  and  $L = 0.2$ ).

### 5.2. Effect of Heat Source Length

The contours of streamline (right) and isotherm (left) of the nanofluid for different values of heated region length ( $L$ ) in the bottom of the semicircular cavity at ( $\phi = 0.02$ ,  $Ha = 50$ ,  $Rd = 0.5$ ,  $Da = 10^{-4}$  and  $Ra = 10^5$ ) are displayed in Figure 7. The results indicated that the stream function reaches its peak value (i.e.,  $\psi = 0.2$ ) at the shorter length of the heated region (i.e.,  $L = 0.1$ ). Consequently, lowering ( $L$ ) is the most effective method of increasing natural convection in the cavity. In fact, the shorter ( $L$ ) decreases the dissipation of thermal energy, and this increases the flow circulation represented by the stream function values. Moreover, it can be noted that both rotating vortices around the internal flame begin to extend and approach each other as ( $L$ ) increases. Moreover, the size of the core of vortices begins to enlarge as ( $L$ ) increases. For isotherm contours, it can be observed that the increase in ( $L$ ) makes two obvious things in their pattern. The first one is that the isotherms above the internal flame moved further towards the upper wall of the cavity. Whereas the other makes a clear divergence between the isotherms, especially adjacent to the heated region in the lower wall. The heated region with the largest ( $L$ ) produces a high heat generation rate and makes the temperature gradient in this region more severe. The temperature and velocity profiles alongside the mean vertical location ( $Y$ ) for different values of ( $L$ ) at ( $\phi = 0.02$ ,  $Ha = 50$ ,  $Rd = 0.5$ ,  $Da = 10^{-4}$  and  $Ra = 10^5$ ) are illustrated respectively in Figure 8a,b. It can be noted that the variation of ( $L$ ) on ( $T$ ) profiles (i.e., Figure 8a) is very slight and approximately similar up to ( $Y = 0.15$ ). But, beyond this value, they decrease along ( $Y$ ), and this decrease becomes more pronounced as ( $L$ ) decreases. For ( $V$ ) profiles (i.e., Figure 8b), a slight variation of them along ( $Y$ ) can be seen up to ( $Y = 0.15$ ). After that, they increase rapidly and decrease gradually to their zero value at ( $Y = 0.2$ ). The peak value of ( $V$ ) profiles corresponds to the shortest heat source length (i.e.,  $L = 0.1$ ).

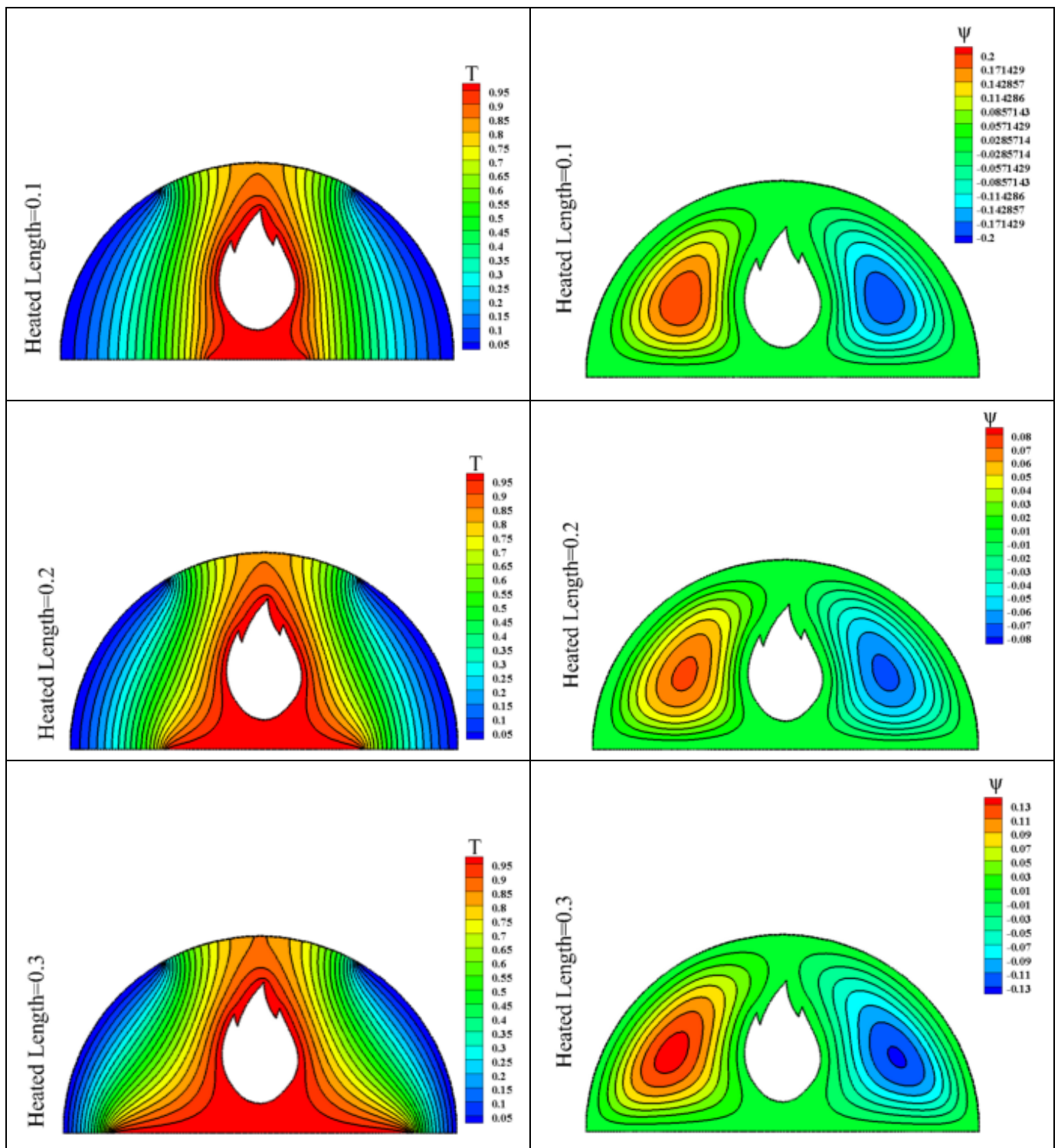
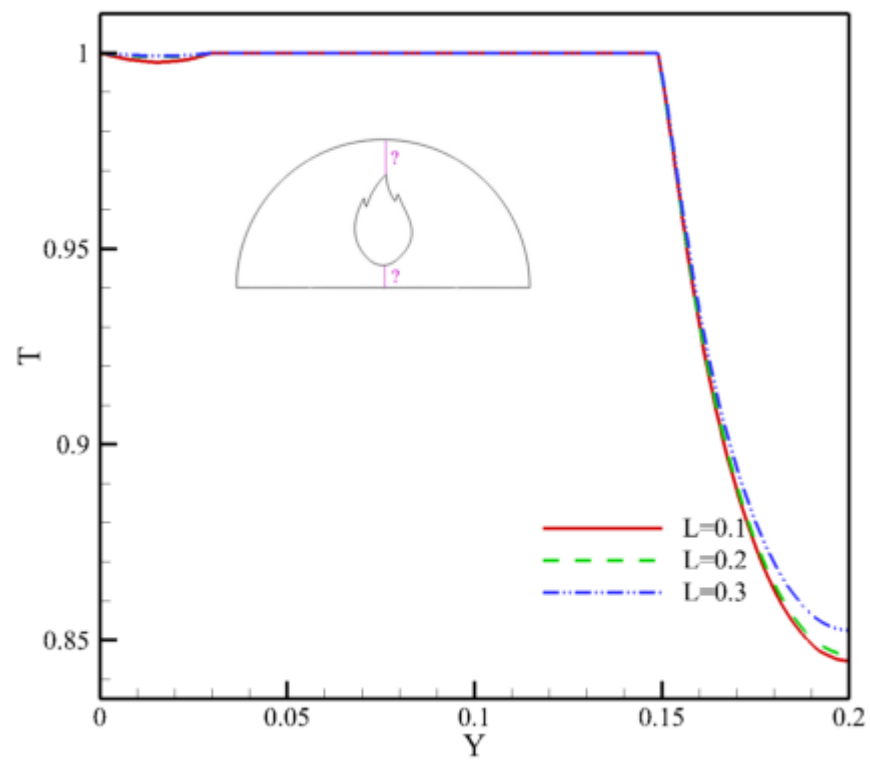
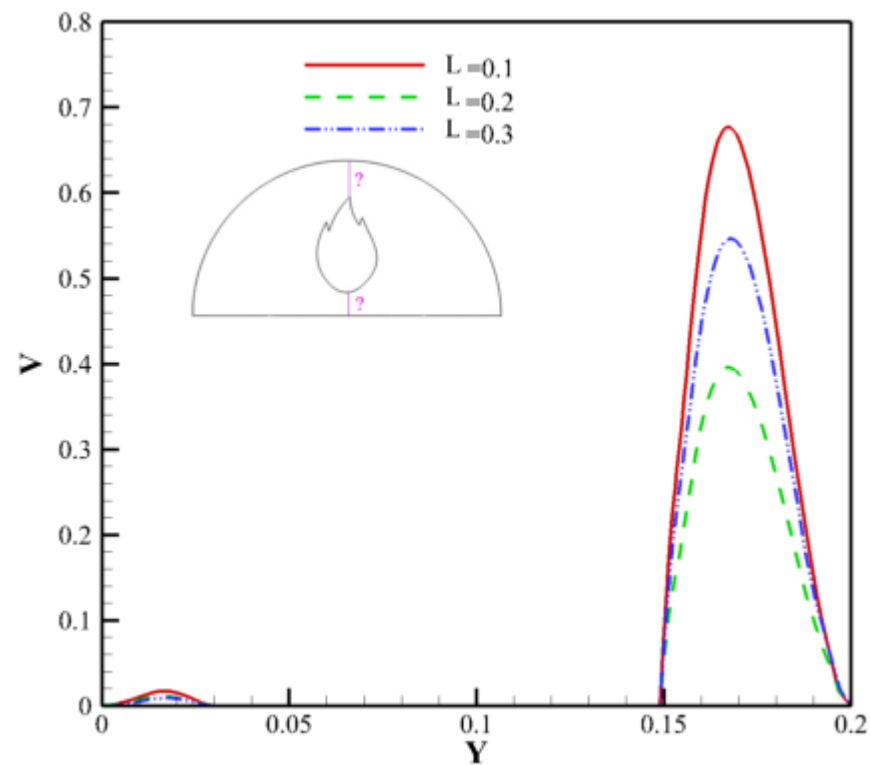


**Figure 7.** Streamlines (right) and isotherms (left) for various values of heated region length in the bottom of the hexagonal enclosure at ( $\phi = 0.02$ ,  $Ha = 50$ ,  $Rd = 0.5$ ,  $Da = 10^{-4}$  and  $Ra = 10^5$ ).



(a)



(b)

**Figure 8.** Variation of (a) temperature alongside mean vertical location (b) velocity alongside mean vertical location for different values for different values of heated length at ( $\phi = 0.02$ ,  $Ha = 50$ ,  $Rd = 0.5$ ,  $Da = 10^{-4}$  and  $Ra = 10^5$ ).

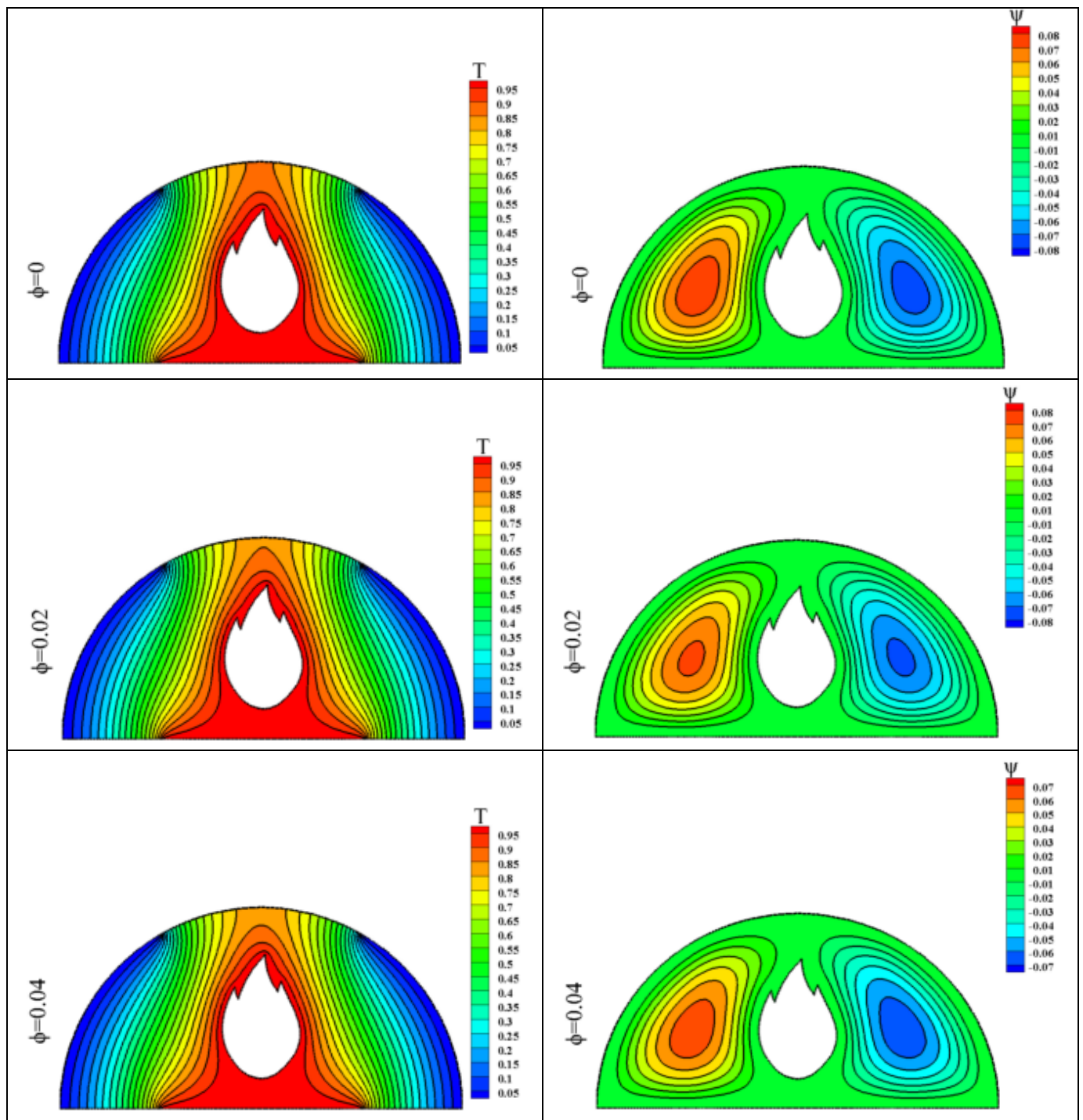
### 5.3. Effect of Solid Volume Fraction

Figure 9 depicts streamline (right) and isotherm (left) contours for various values of  $(\phi)$  at  $(Rd = 0.5, Ha = 50, L = 0.2, Da = 10^{-4}$  and  $Ra = 10^5)$ . The result explains that the increase in  $(\phi)$  leads to damping of the stream function values. So, the lowest value of it (i.e.,  $\psi = 0.07$ ) corresponds to  $(\phi = 0.04)$ . This is due to the rise in the viscosity of nanofluid for the highest value of  $(\phi)$ , which impedes the simplicity of the flow circulation in the cavity. Moreover, the increase of  $(\phi)$  leads to enlarging the cores of rotating vortices. With respect to isotherms, it can be noted that the increase in  $(\phi)$  has a trivial effect on their pattern. This can be confirmed by high matching between them when  $(\phi)$  increases from  $(\phi = 0)$  to  $(\phi = 0.04)$ . The only difference between them can be observed in the spot above the internal flame, where the isotherm lines begin to back down with the increase in  $(\phi)$ . The variation of  $(Nu_{out})$  at the heated wall of the cavity, temperature and velocity profiles alongside the mean vertical location for different values of  $(\phi)$  at  $(Rd = 0.5, Ha = 50, L = 0.2, Da = 10^{-4}$  and  $Ra = 10^5)$  are depicted respectively in Figure 10a–c. As expected, the increase in  $(\phi)$  leads to enhanced  $(Nu_{out})$  values. Therefore, the nanofluid  $(\phi = 0.04)$  is better than the water  $(\phi = 0)$  and can be used to enhance the natural convection in the cavity. This is due to the increase in thermal conductivity of the water caused by the addition of SWCNTs nanoparticles. Furthermore, the increase in  $(X)$  leads to a decrease  $(Nu_{out})$  until a certain value and then increases with the increase in  $(X)$  for all values of  $(\phi)$ . Similar to the behaviour discussed previously in Figure 6b, the  $(T)$  linearly varies until  $(Y = 0.15)$ , and a severe drop was noted after that. On the other hand, a slight variation of  $(V)$  along  $(Y)$  can be noted from Figure 10c until  $(Y = 0.15)$ . Then,  $(V)$  increases to a specified value before it decreases again up to  $(Y = 0.2)$ . For all values of  $(Y)$ , both  $(T)$  and  $(V)$  increase with the decrease in  $(\phi)$ .

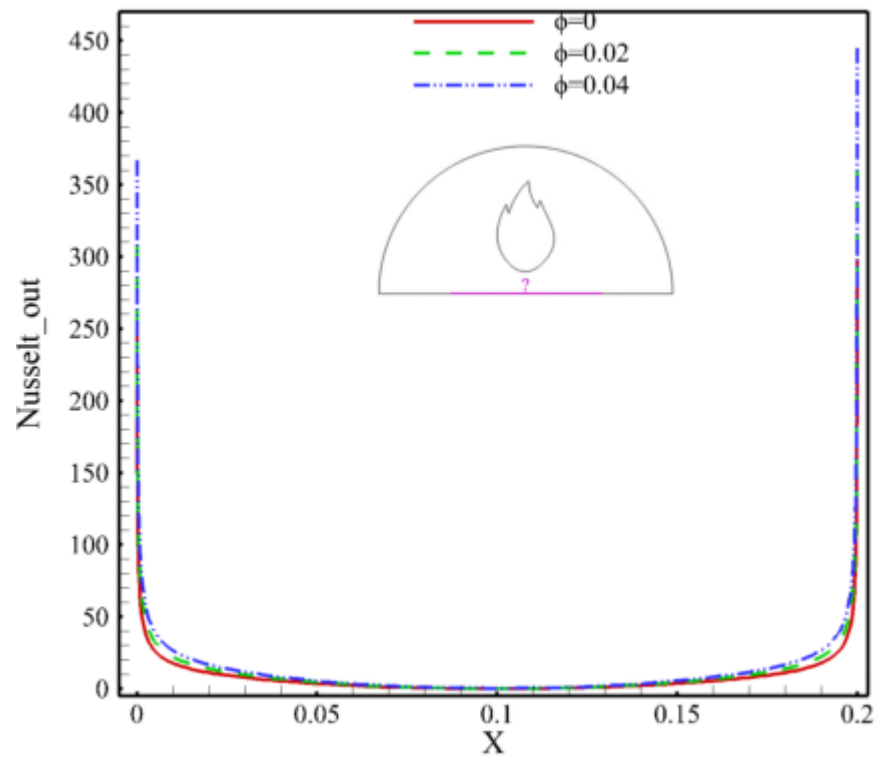
### 5.4. Effect of Hartmann Number

Both the streamlines (right) and isotherms (left) for various values of  $(Ha)$  at  $(\phi = 0.02, L = 0.2, Rd = 0.5, Da = 10^{-4}$  and  $Ra = 10^5)$  are illustrated in Figure 11. In fact, the intensity of the magnetic field can be measured through  $(Ha)$ . The results indicated that the maximum stream function value decreases from  $(\psi = 0.08)$  at  $(Ha = 0)$  to  $(\psi = 0.05)$  at  $(Ha = 100)$ . Therefore, it can be deduced that the existence of a magnetic field with high strength (i.e.,  $Ha = 100$ ) causes a drop and a clear deceleration in the flow circulation compared with the case of no applied magnetic field  $(Ha = 0)$ . This deceleration can be attributed to the Lorentz force influence (generated by the magnetic field), which becomes more dominant than the buoyancy force. As a result, it may be deduced that the magnetic field reduces the intensity of the natural convection within the cavity. Moreover, increase in  $(Ha)$  leads the rotating vortices to extend further inside the cavity and approach each other, especially at  $(Ha = 100)$ . In terms of the thermal field, it is worth noting that a rise in  $(Ha)$  has only a little influence on the contours of isothermal curves. This observation can be supported by the high similarity of their pattern for various values of  $(Ha)$ . Figure 12a–c shows the variation of  $(Nu_{out})$  at the heated wall of the cavity, temperature and velocity profiles alongside the mean vertical location for different values of  $(Ha)$  at  $(\phi = 0.02, L = 0.2, Rd = 0.5, Da = 10^{-4}$  and  $Ra = 10^5)$ . It can be noted from (Figure 12a) that for all values of  $(Ha)$ ,  $(Nu_{out})$  decreases with the increase in  $(X)$  until  $(X = 0.1)$  and then increases beyond this value. Furthermore, the increase in  $(Ha)$  leads to a decrease in  $(Nu_{out})$ . This is due to weak natural convection caused by increasing the magnetic field, which leads to a decrease in the buoyancy force and damps  $(Nu_{out})$ . So, the  $(Nu_{out})$  attains its peak value at  $(Ha = 0)$ . Figure 12b,c illustrates both the temperature and velocity profiles, respectively, alongside the mean vertical location for different values of  $(Ha)$ . It may be noted from (Figure 12b) that there is a linear variation between  $(T)$  and  $(Y)$  until a certain value and a severe drop in  $(T)$  profiles was noted after this value. The increase in  $(Ha)$  leads to a decrease in  $(T)$  profiles, as shown in the block zoom in Figure 12b. In the same manner, the  $(V)$  profile varies slightly along  $(Y)$  until a certain value and then increases strongly until it reaches its

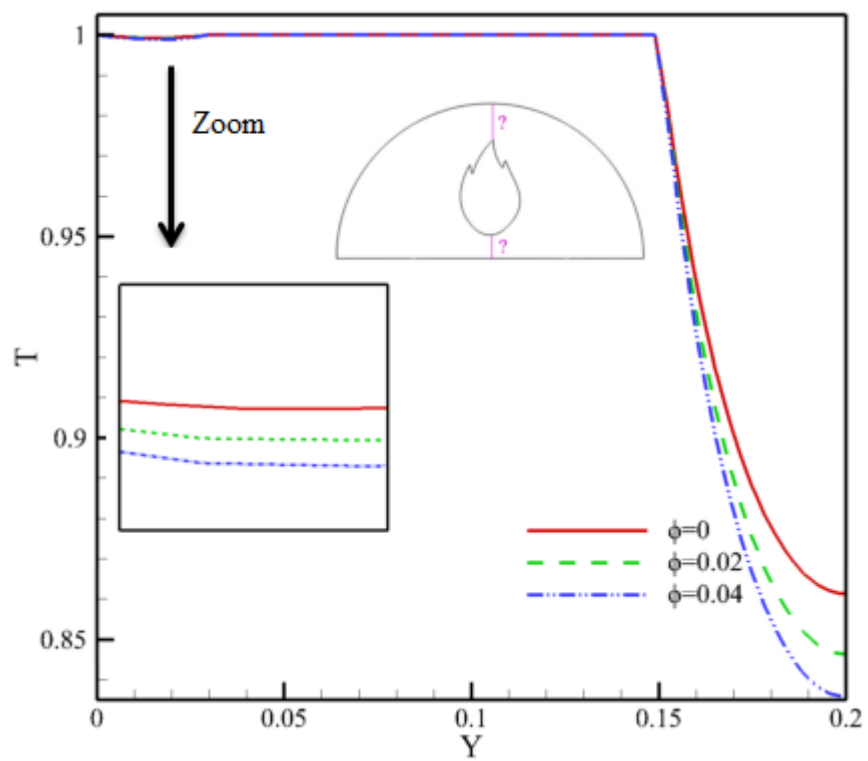
maximum value at ( $Y = 0.17$ ). Then, it decreases gradually until it reaches its zero value at ( $Y = 0.2$ ). Again, the increase in ( $Ha$ ) decreases ( $V$ ) profiles.



**Figure 9.** Streamlines (right) and isotherms (left) in the enclosure for different values of solid volumetric fraction at ( $Rd = 0.5, Ha = 50, L = 0.2, Da = 10^{-4}$  and  $Ra = 10^5$ ).



(a)



(b)

Figure 10. Cont.

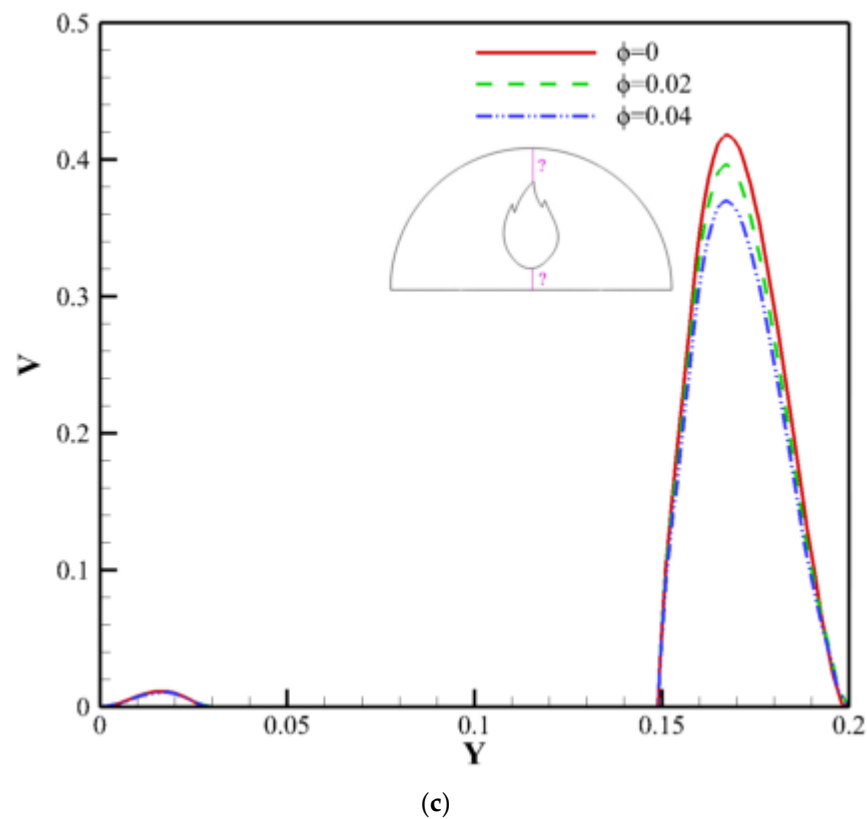


**Figure 10.** Variation of (a) Nusselt number at the enclosure heated length, (b) temperature along vertically mean position and (c) velocity alongside mean vertical location for different values of  $\phi$  at ( $Rd = 0.5$ ,  $Ha = 50$ ,  $L = 0.2$ ,  $Da = 10^{-4}$  and  $Ra = 10^5$ ).

### 5.5. Effect of Radiation Parameter

Figure 13 depicts the streamlines (right) and isotherms (left) of the nanofluid inside the semicircular cavity for various values of ( $Rd$ ) at ( $\phi = 0.02$ ,  $L = 0.2$ ,  $Ha = 50$ ,  $Da = 10^{-4}$  and  $Ra = 10^5$ ). It may be noted that at ( $Rd = 0.5$ ), the maximum stream function reaches its peak value (i.e.,  $\psi = 0.08$ ). So, this value can be considered as an optimum one for improving the natural convection in the cavity compared with the case of no radiation (i.e.,  $Rd = 0$ ) and ( $Rd = 1$ ). Moreover, the increase in ( $Rd$ ) results in increasing the core size for both hot and cold rotating vortices. From the other side, the isotherm contours indicate that the increase in ( $Rd$ ) causes an increase in the region's temperature above the internal flame. Figure 14a–c illustrate respectively the profiles of ( $Nu_{out}$ ), ( $T$ ) and ( $V$ ) for various values of ( $Rd$ ) at ( $\phi = 0.02$ ,  $L = 0.2$ ,  $Ha = 50$ ,  $Da = 10^{-4}$  and  $Ra = 10^5$ ). The results indicated that an increase in ( $Rd$ ) increases the ( $Nu_{out}$ ). Since the radiation positively affects the natural convection, which leads to this increase in ( $Nu_{out}$ ). The latter drops with ( $X$ ) until a limited value, and then an increase can be noted. This behaviour is repeated for all values of ( $Rd$ ). With respect to the effect of ( $Rd$ ) on both ( $T$ ) and ( $V$ ) profiles, it was noted that ( $T$ ) increases with the increase in ( $Rd$ ). At the same time, its effect on ( $V$ ) is very minor. This behaviour was seen for ( $0.15 \leq Y \leq 0.2$ ).

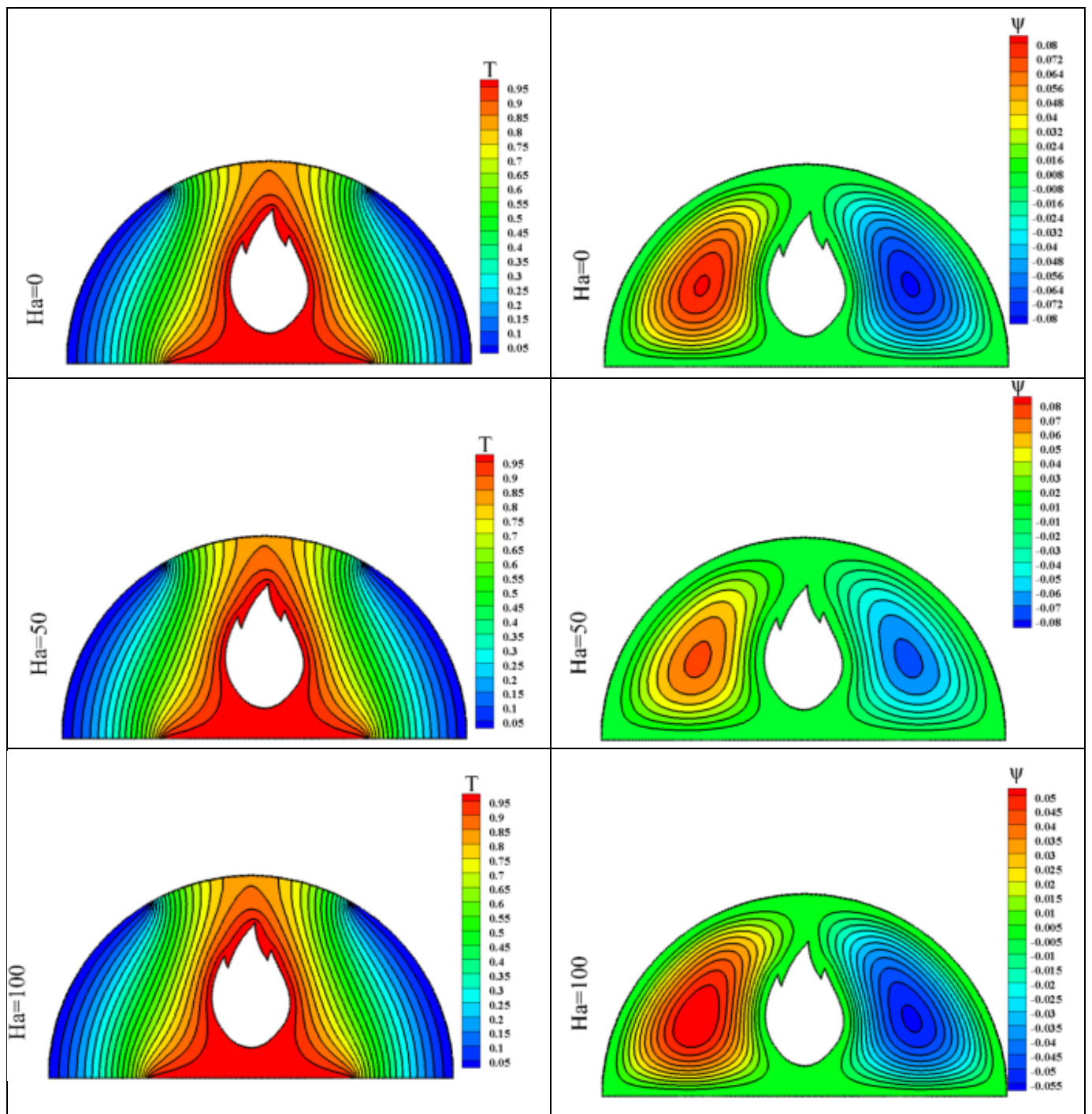
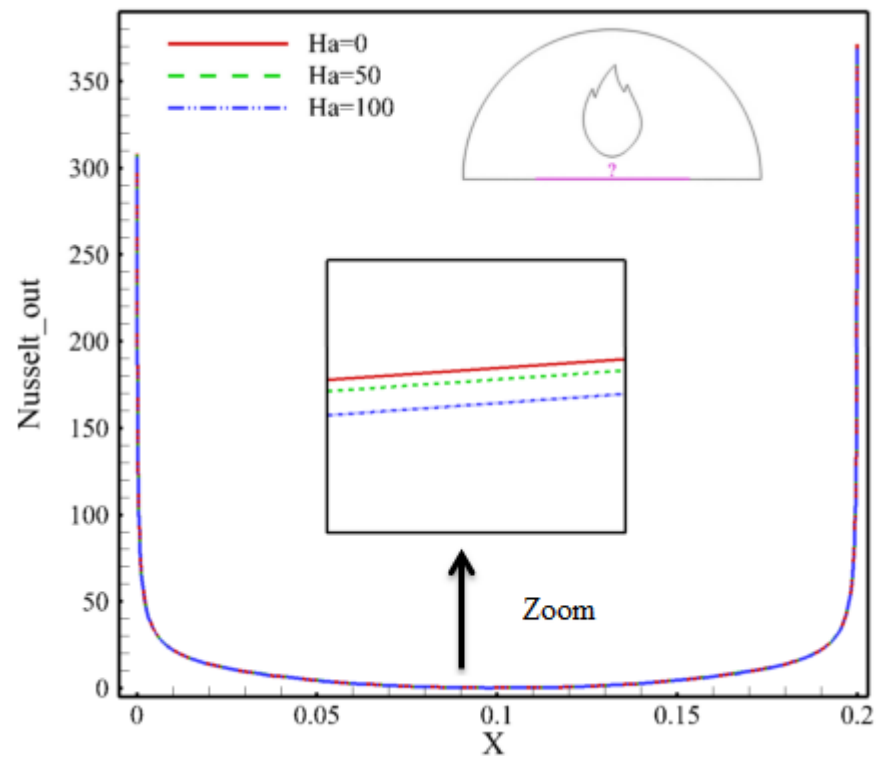
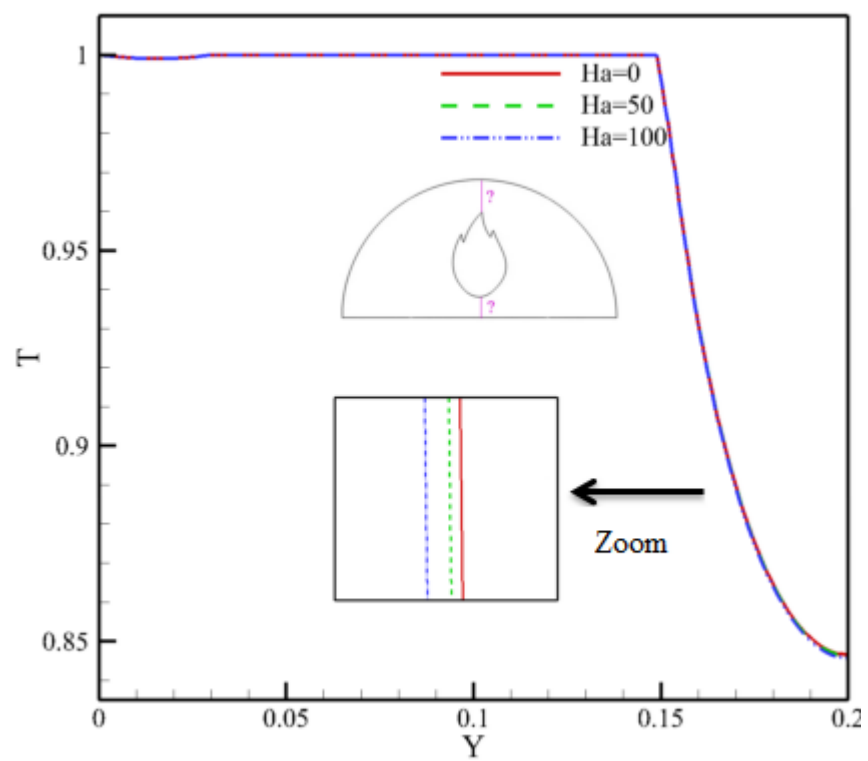


**Figure 11.** Streamlines (**right**) and isotherms (**left**) inside the enclosure for various values of Ha at ( $\phi = 0.02$ ,  $L = 0.2$ ,  $Rd = 0.5$ ,  $Da = 10^{-4}$  and  $Ra = 10^5$ ).



(a)



(b)

Figure 12. Cont.

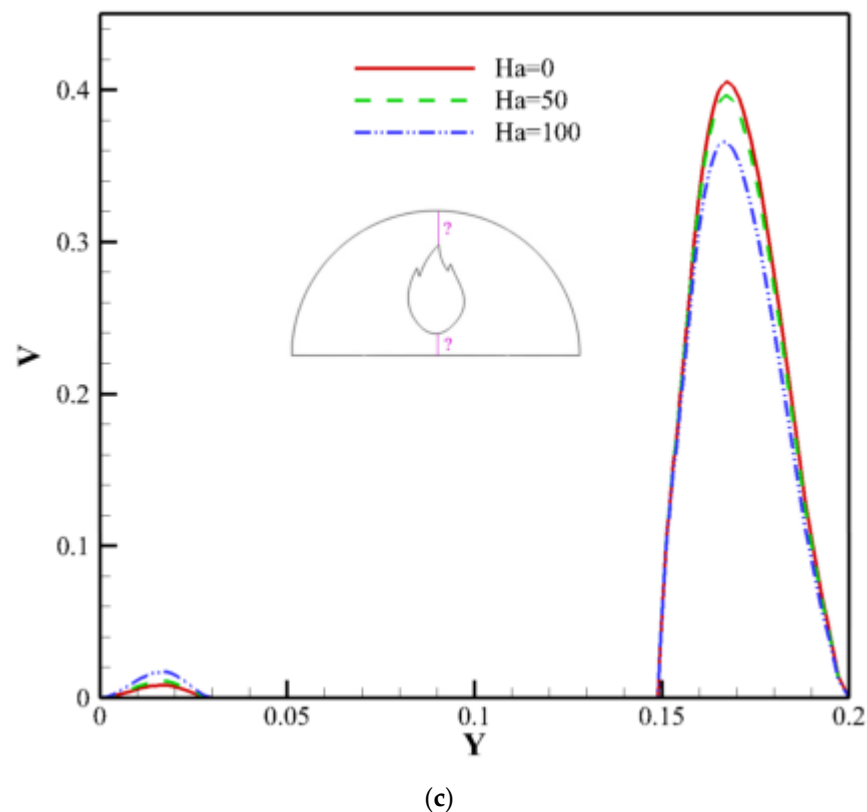


**Figure 12.** Variation of (a) Nusselt number at the enclosure heated length, (b) temperature along vertically mean position and (c) velocity alongside mean vertical location for different values of (Ha) at ( $\phi = 0.02$ ,  $L = 0.2$ ,  $Rd = 0.5$ ,  $Da = 10^{-4}$  and  $Ra = 10^5$ ).

### 5.6. Effect of Darcy Number

Figure 15 shows streamlines (right) and isotherms (left) of the nanofluid inside the semicircular cavity for various values of (Da) at ( $\phi = 0.02$ ,  $L = 0.2$ ,  $Rd = 0.5$ ,  $Ha = 50$  and  $Ra = 10^5$ ). The decrease in (Da) decreases the maximum stream function value from ( $\psi = 0.2$ ) at ( $Da = 10^{-3}$ ) to ( $\psi = 0.01$ ) at ( $Da = 10^{-5}$ ). Since the decrease in it decreases the permeability of the porous media and increases its resistance to the flow circulation. Therefore, the flow vortices move more slowly inside the cavity, and as a result, the stream function values decrease. So, it can be deduced that the increase in (Da) enhances the natural convection inside the cavity. Moreover, the decrease in (Da) makes both rotating vortices around the internal flame approach each other. With respect to the effect of (Da) on isotherms, it was noted that the decrease in it makes them move back from the upper wall of the cavity. Figure 16a–c displays respectively the profiles of ( $Nu_{out}$ ), (T) and (V) alongside the mean vertical location for different values of (Da) at ( $\phi = 0.02$ ,  $L = 0.2$ ,  $Rd = 0.5$ ,  $Ha = 50$  and  $Ra = 10^5$ ). As explained previously, ( $Nu_{out}$ ) decreases with the decrease in (Da). Moreover, it decreases gradually along (X) until ( $X = 0.1$ ) and increases after that. With respect to (T) profiles (Figure 16b), it was observed that they vary linearly along (Y) until ( $Y = 0.15$ ), and the lowest value of them corresponds to ( $Da = 10^{-3}$ ). While, a remarkable decrease in (T) along (Y) can be noted after ( $Y = 0.15$ ), and it increases with the increase in (Da). For Figure 16c, the (V) profiles vary very slightly with (Y) until a certain value and then jump strongly after that. This jump in (V) profiles decreases with the decrease in (Da) from ( $Da = 10^{-3}$ ) to ( $Da = 10^{-5}$ ). Then, as expected, the (V) profiles reach zero value at ( $Y = 0.2$ ).

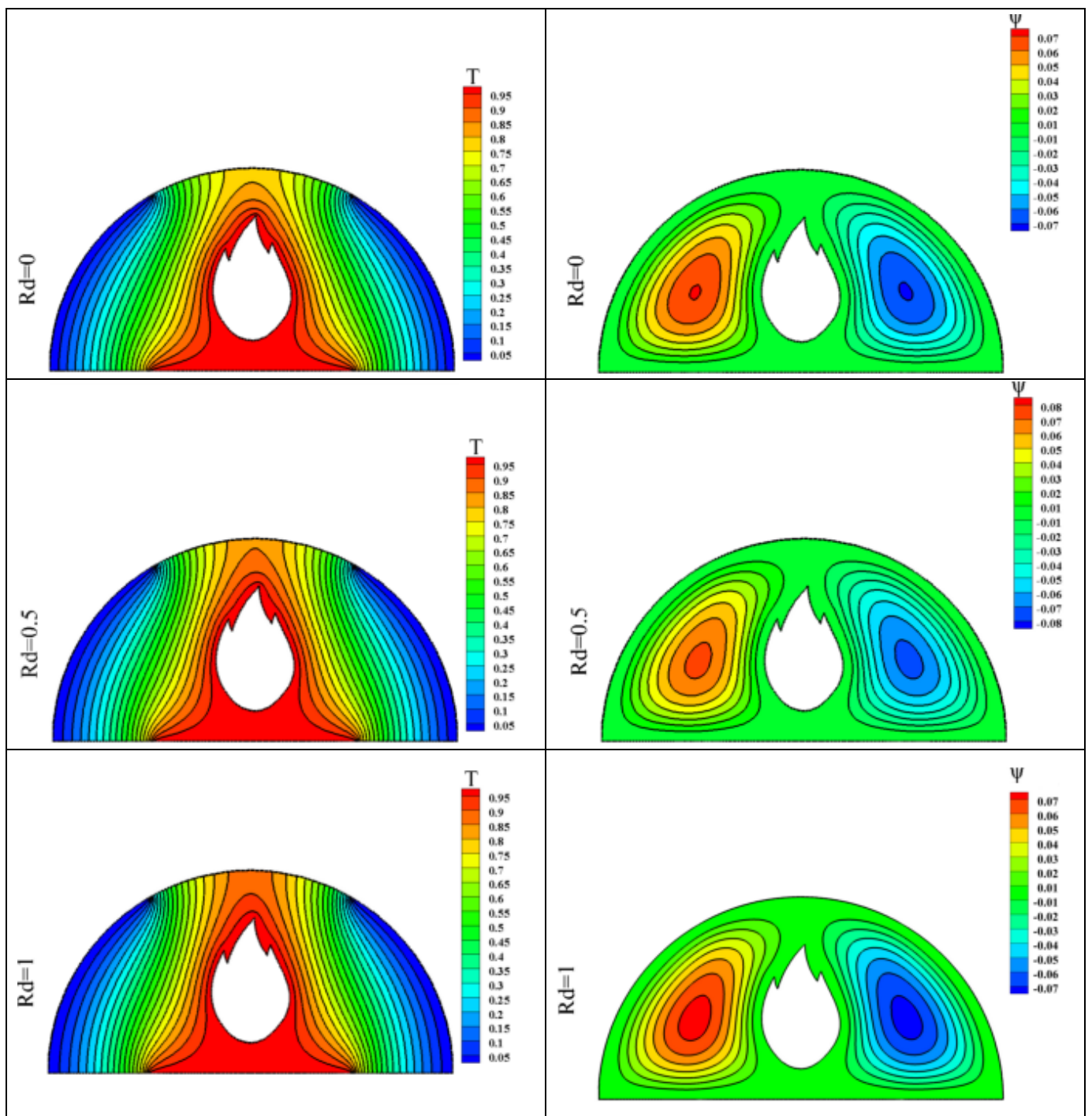
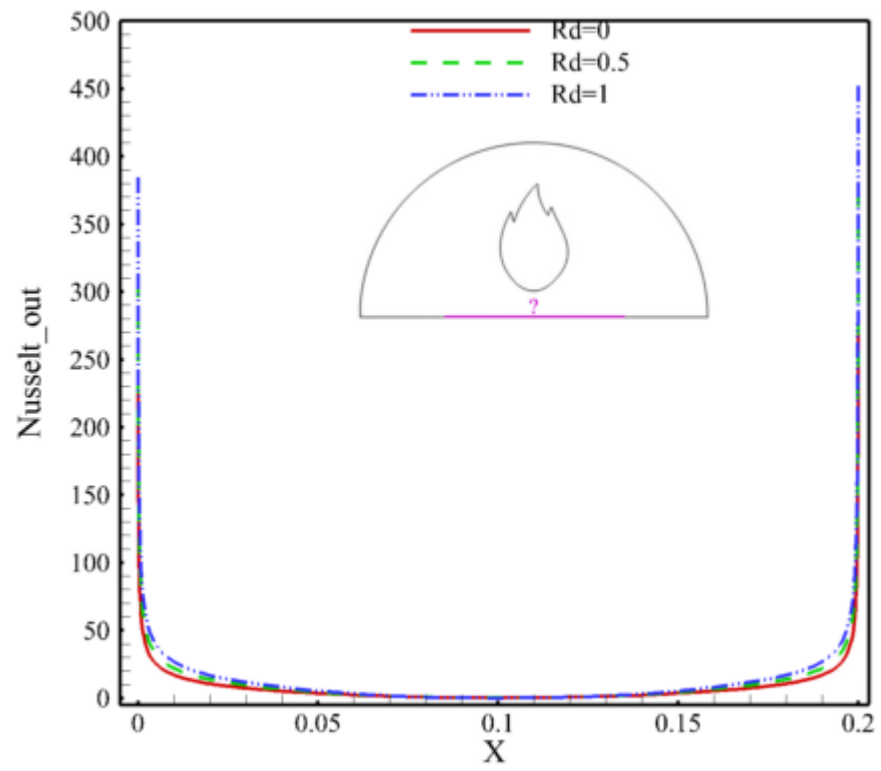
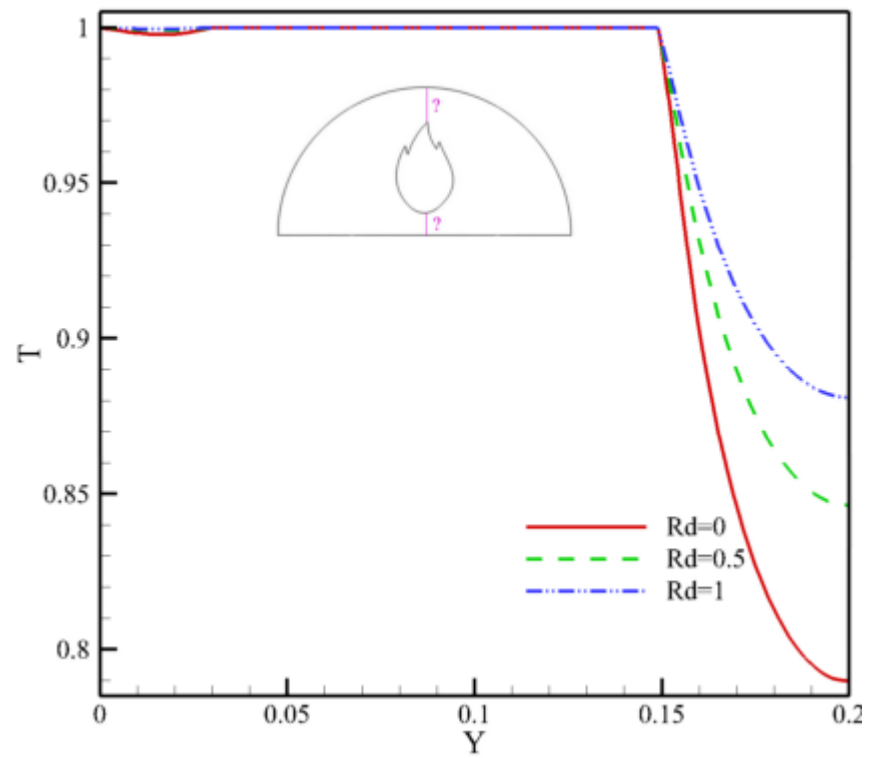


**Figure 13.** Streamlines (right) and isotherms (left) inside the enclosure for various values of radiation parameter at ( $\phi = 0.02$ ,  $L = 0.2$ ,  $Ha = 50$ ,  $Da = 10^{-4}$  and  $Ra = 10^5$ ).



(a)



(b)

Figure 14. Cont.

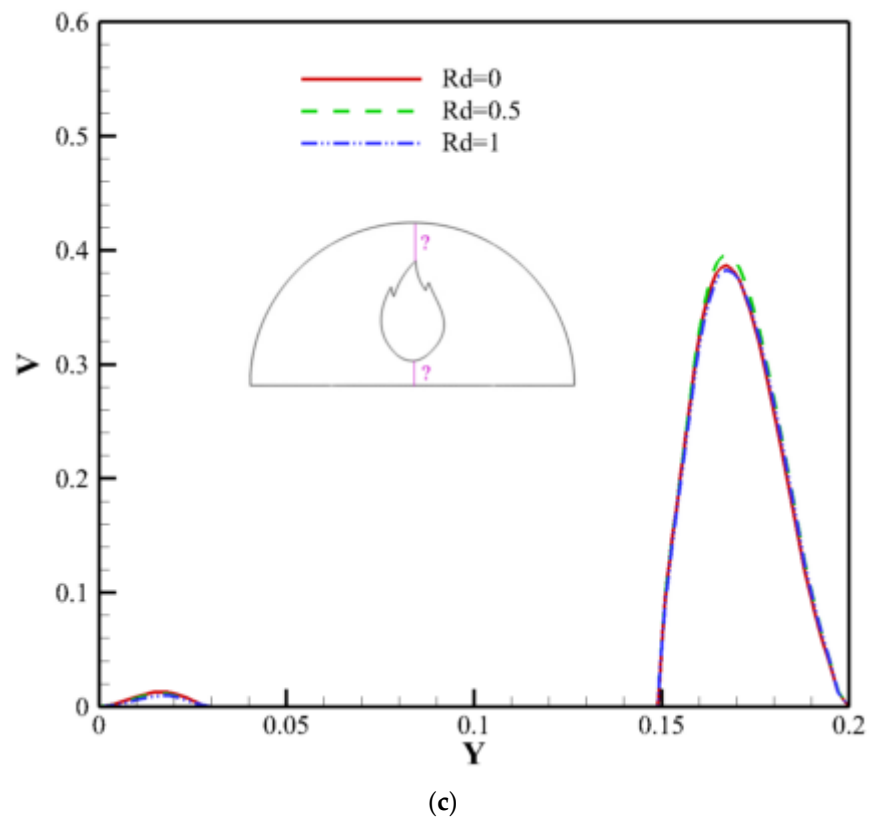


**Figure 14.** Variation of (a) Nusselt number at the enclosure heated length, (b) temperature along vertically mean position and (c) velocity alongside mean vertical location for different values of  $Rd$  at ( $\phi = 0.02$ ,  $L = 0.2$ ,  $Ha = 50$ ,  $Da = 10^{-4}$  and  $Ra = 10^5$ ).

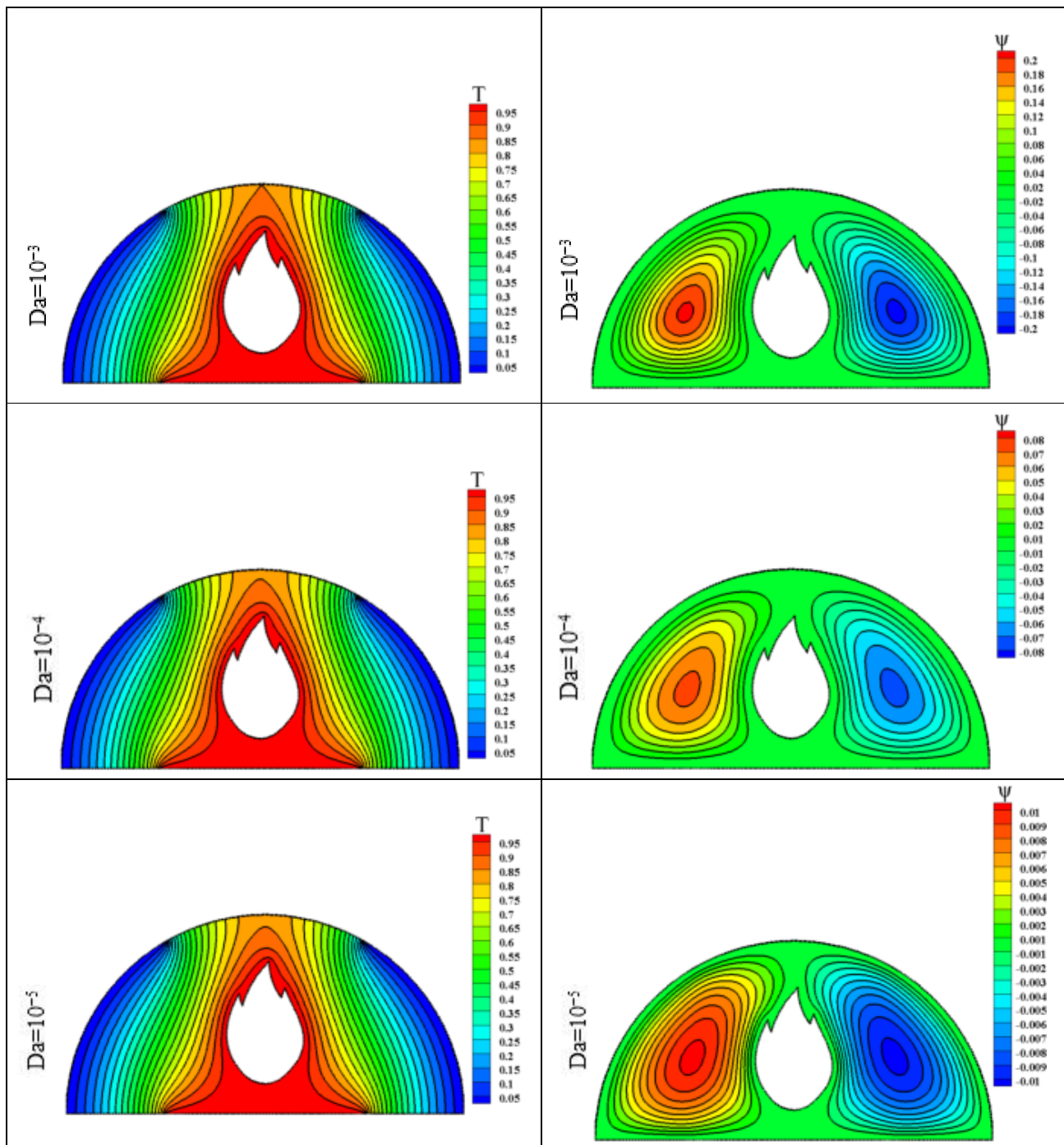
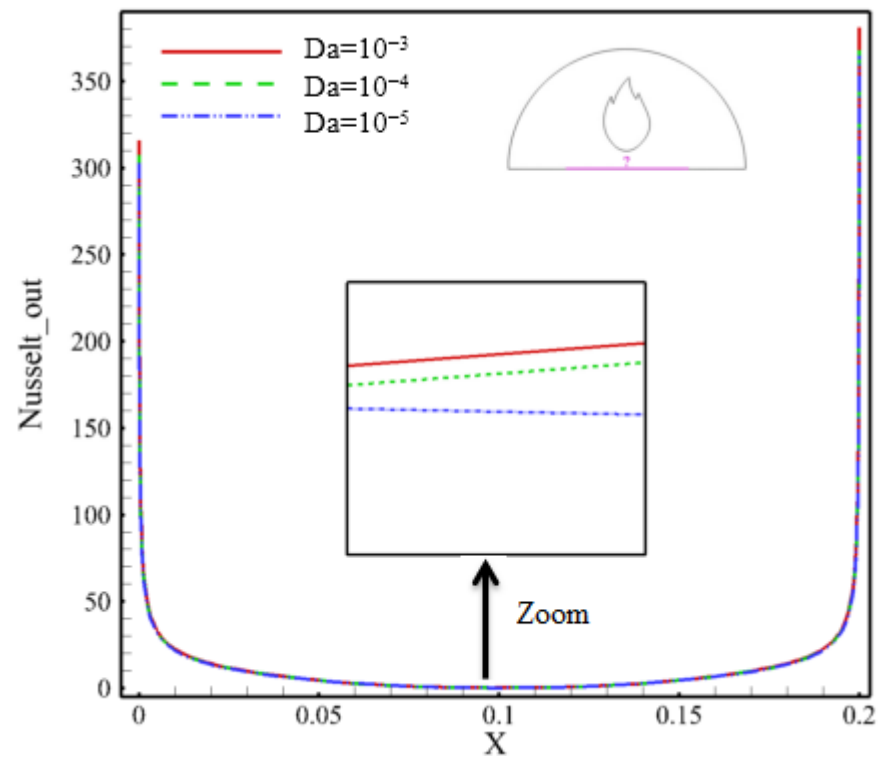
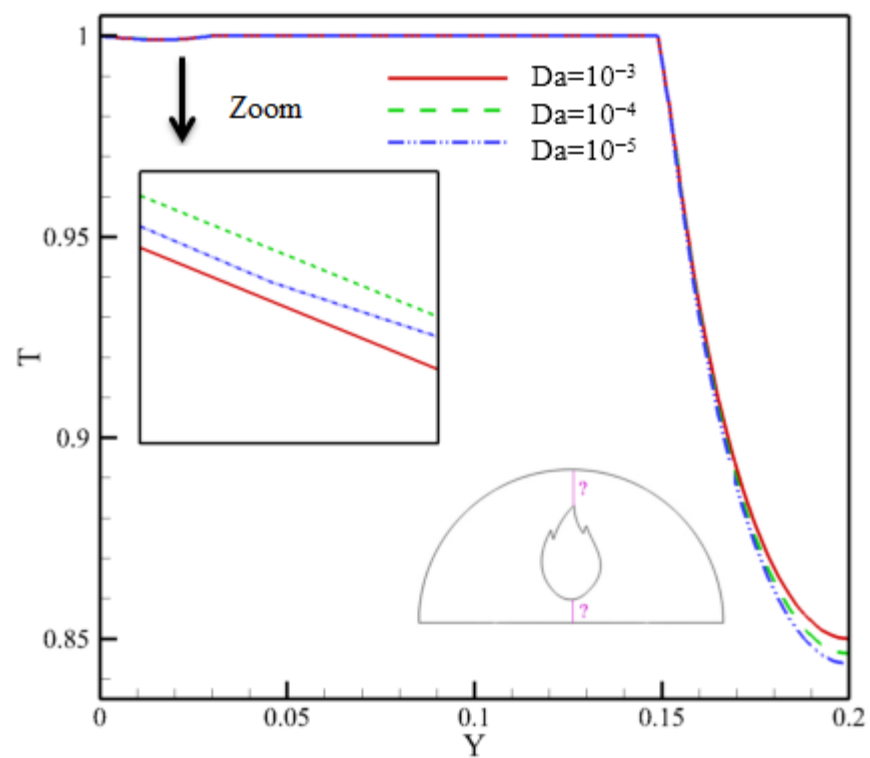


**Figure 15.** Streamlines (right) and isotherms (left) inside the enclosure for various values of Da at ( $\phi = 0.02$ ,  $L = 0.2$ ,  $Ha = 50$  and  $Ra = 10^5$ ).



(a)



(b)

Figure 16. Cont.

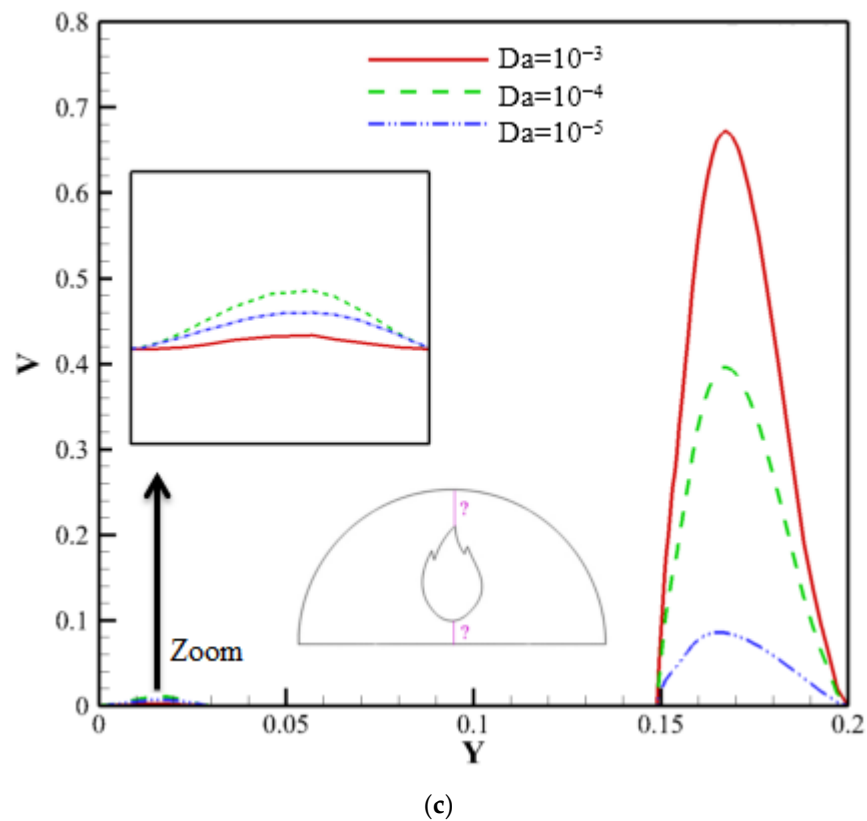


**Figure 16.** Variation of (a) Nusselt number at the enclosure heated length, (b) temperature alongside mean vertical location and (c) velocity alongside mean vertical location for different values of  $Da$  at ( $\phi = 0.02$ ,  $L = 0.2$ ,  $Ha = 50$  and  $Ra = 10^5$ ).

## 6. Conclusions

According to the findings of the current study, the following conclusions may be reached:

- The increase in ( $Ra$ ) leads to an increase in the natural convection effect.
- Both ( $Nu_{out}$ ) and ( $V$ ) increase as ( $Ra$ ) increases.
- The ( $T$ ) profiles vary approximately linearly along ( $Y$ ) up to ( $Y = 0.15$ ) and increase with a decrease in ( $Ra$ ). After that, they begin to drop sharply and increase with the increase in it.
- A decrease in ( $L$ ) improves the natural convection within the cavity.
- A symmetrical ( $T$ ) profile is seen up to ( $Y = 0.15$ ), while they decrease along ( $Y$ ) as ( $L$ ) decreases.
- The increase in ( $\phi$ ) damps the stream function values. While its effect on isotherms is slight except in the spot above the internal flame.
- ( $Nu_{out}$ ) increases when nanofluid is used instead of water.
- For all values of ( $Y$ ), both ( $T$ ) and ( $V$ ) increase with the decrease in ( $\phi$ ).
- The increase in ( $Ha$ ) decreases both the flow circulation ( $Nu_{out}$ ), ( $T$ ) and ( $V$ ) profiles.
- The increase in ( $Rd$ ) increases the ( $Nu_{out}$ ). For ( $0.15 \leq Y \leq 0.2$ ), the increase in ( $Rd$ ) increases ( $T$ ), whereas its effect on ( $V$ ) is slight.
- The decrease in ( $Da$ ) decreases the maximum stream function value.
- ( $Nu_{out}$ ) decreases with the decrease in ( $Da$ ). While ( $T$ ) profiles decrease along ( $Y$ ) after ( $Y = 0.15$ ), they increase with the increase in ( $Da$ ). For ( $V$ ) profiles, they jump after ( $Y = 0.15$ ) and decrease with the decrease in ( $Da$ ).
- Increasing ( $Rd$ ) enhances the average  $Nu$  on the heated length by about (56.55%) and causes an augmentation of about (73%) in the average  $Nu$  on heated flame.
- Raising ( $Ha$ ) augments the maximum  $Y$ -velocity by about (82.4%).

- The present work results can be used in many industrial applications such as solar energy systems.

**Author Contributions:** Conceptualization, M.A. and A.K.H.; methodology, O.Y., A.K.H. and B.A.; software, E.H.M. and U.B.; validation, O.Y. and A.K.H.; formal analysis, O.Y., U.B. and M.A.; investigation, A.K.H. and B.A.; resources, U.B. and O.Y.; data curation, E.H.M. and A.K.H.; writing—original draft preparation, O.Y., M.A., A.K.H., B.A. and U.B.; writing—review and editing, E.H.M. and M.A.; project administration, A.K.H.; funding acquisition, O.Y. All authors have read and agreed to the published version of the manuscript.

**Funding:** This research was funded by the Deputyship for Research & Innovation, Ministry of Education in Saudi Arabia grant number [IF-PSAU-2021/01/17645].

**Institutional Review Board Statement:** Not applicable.

**Informed Consent Statement:** Not applicable.

**Data Availability Statement:** Not applicable.

**Acknowledgments:** The authors extend their appreciation to the Deputyship for Research & Innovation, Ministry of Education in Saudi Arabia, for funding this research work through the project number (IF-PSAU-2021/01/17645).

**Conflicts of Interest:** The authors declare no conflict of interest.

## References

- Choi, S. Enhancing thermal conductivity of fluids with nanoparticles. In Proceedings of the ASME International Mechanical Engineering Congress & Exposition, San Francisco, CA, USA, 12–17 November 1995; ASME Publ-Fed: New York, NY, USA, 1995; Volume 231, pp. 99–106.
- Mahmoudi, A.; Shahi, M.; Raouf, A.; Ghasemian, A. Numerical study of natural convection cooling of horizontal heat source mounted in a square cavity filled with nanofluid. *Int. Commun. Heat Mass Transf.* **2010**, *37*, 1135–1141. [[CrossRef](#)]
- Sandhya, D.; Reddy, M.S.; Rao, V. Improving the cooling performance of automobile radiator with ethylene glycol water-based TiO<sub>2</sub> nanofluids. *Int. Commun. Heat Mass Transf.* **2016**, *78*, 121–126.
- Moraveji, M.; Hejazian, M. Natural convection in a rectangular enclosure containing an oval-shaped heat source and filled with Fe<sub>3</sub>O<sub>4</sub>/water nanofluid. *Int. Commun. Heat Mass Transf.* **2013**, *44*, 135–146. [[CrossRef](#)]
- Sajid, M.; Ali, H. Recent advances in application of nanofluids in heat transfer devices: A critical review. *Renew. Sustain. Energy Rev.* **2019**, *103*, 556–592. [[CrossRef](#)]
- Kamel, M.; Lezsovits, F.; Hussein, A.K. Experimental studies of flow boiling heat transfer by using nanofluids: A recent critical review. *J. Therm. Anal. Calorim.* **2019**, *138*, 4019–4043. [[CrossRef](#)]
- Pordanjani, A.; Aghakhani, S.; Afrand, M.; Mahmoudi, B.; Mahian, O.; Wongwises, S. An updated review on application of nanofluids in heat exchangers for saving energy. *Energy Convers. Manag.* **2019**, *198*, 111886. [[CrossRef](#)]
- Corvaro, F.; Paroncini, M.; Sotte, M. Experimental PIV and interferometric analysis of natural convection in a square enclosure with partially active hot and cold walls. *Int. J. Therm. Sci.* **2011**, *50*, 1629–1638. [[CrossRef](#)]
- Garoosi, F.; Bagheri, G.; Talebi, F. Numerical simulation of natural convection of nanofluids in a square cavity with several pairs of heaters and coolers (HACs) inside. *Int. J. Heat Mass Transf.* **2013**, *67*, 362–376. [[CrossRef](#)]
- Wakashima, S.; Saitoh, T. Benchmark solutions for natural convection in a cubic cavity using the high-order time-space method. *Int. J. Heat Mass Transf.* **2004**, *47*, 853–864. [[CrossRef](#)]
- Bouchta, S.; Feddaoui, M.; El-Ihssini, H. Natural convection in a square cavity containing a nanofluid and a partially-heated square block at the centre. *Am. J. Heat Mass Transf.* **2017**, *4*, 40–52. [[CrossRef](#)]
- Rashidi, I.; Mahian, O.; Lorenzini, G.; Biserni, C.; Wongwises, S. Natural convection of Al<sub>2</sub>O<sub>3</sub>-water nanofluid in a square cavity: Effects of heterogeneous heating. *Int. J. Heat Mass Transf.* **2014**, *74*, 391–402. [[CrossRef](#)]
- Samadzadeh, A.; Heris, S.; Hashim, I.; Mahian, O. An experimental investigation on natural convection of non-covalently functionalized MWCNTs nanofluids: Effects of aspect ratio and inclination angle. *Int. Commun. Heat Mass Transf.* **2020**, *111*, 104473. [[CrossRef](#)]
- Kefayati, G. Effect of a magnetic field on natural convection in an open cavity subjugated to water/alumina nanofluid using Lattice Boltzmann method. *Int. Commun. Heat Mass Transf.* **2013**, *40*, 67–77. [[CrossRef](#)]
- Ashorynejad, H.; Shahriari, A. MHD natural convection of hybrid nanofluid in an open wavy cavity. *Results Phys.* **2018**, *9*, 440–455. [[CrossRef](#)]
- Gangawane, K. Effect of the angle of applied magnetic field on natural convection in an open-ended cavity with partially active walls. *Chem. Eng. Res. Des.* **2017**, *127*, 22–34. [[CrossRef](#)]

17. Miroshnichenko, I.; Sheremet, M.; Oztop, H.; Al-Salem, K. MHD natural convection in a partially open trapezoidal cavity filled with a nanofluid. *Int. J. Mech. Sci.* **2016**, *119*, 294–302. [[CrossRef](#)]
18. Astanina, M.; Sheremet, M.; Oztop, H.; Abu-Hamdeh, N. MHD natural convection and entropy generation of ferrofluid in an open trapezoidal cavity partially filled with a porous medium. *Int. J. Mech. Sci.* **2018**, *136*, 493–502. [[CrossRef](#)]
19. Mahmoudi, A.; Pop, I.; Shahi, M. Effect of magnetic field on natural convection in a triangular enclosure filled with nanofluid. *Int. J. Therm. Sci.* **2012**, *59*, 126–140. [[CrossRef](#)]
20. Sheikholeslami, M.; Gorji-Bandpy, M.; Ganji, D.; Soleimani, S. Effect of a magnetic field on natural convection in an inclined half-annulus enclosure filled with Cu-water nanofluid using CVFEM. *Adv. Powder Technol.* **2013**, *24*, 980–991. [[CrossRef](#)]
21. Mansour, M.; Bakier, A.; Bakeir, M. MHD natural convection in the localized heat sources of an inclined trapezoidal nanofluid-filled enclosure. *Am. J. Eng. Res.* **2013**, *2*, 140–161.
22. Sheikholeslami, M.; Gorji-Bandpy, M.; Ganji, D. Numerical investigation of MHD effects on Al<sub>2</sub>O<sub>3</sub>-water nanofluid flow and heat transfer in a semi-annulus enclosure using LBM. *Energy* **2013**, *60*, 501–510. [[CrossRef](#)]
23. Aminossadati, S. Hydromagnetic natural cooling of a triangular heat source in a triangular cavity with water-CuO nanofluid. *Int. Commun. Heat Mass Transf.* **2013**, *43*, 22–29. [[CrossRef](#)]
24. Elshehabe, H.; Hady, F.; Ahmed, S.; Mohamed, R. Numerical investigation for natural convection of a nanofluid in an inclined L-shaped cavity in the presence of an inclined magnetic field. *Int. Commun. Heat Mass Transf.* **2014**, *57*, 228–238. [[CrossRef](#)]
25. Al-Zamily, A. Effect of magnetic field on natural convection in a nanofluid-filled semicircular enclosure with heat flux source. *Comput. Fluids* **2014**, *103*, 71–85. [[CrossRef](#)]
26. Sheikholeslami, M.; Gorji-Bandpy, M.; Ganji, D.; Soleimani, S. Natural convection heat transfer in a cavity with sinusoidal wall filled with CuO-water nanofluid in presence of magnetic field. *J. Taiwan Inst. Chem. Eng.* **2014**, *45*, 40–49. [[CrossRef](#)]
27. Sheikholeslami, M.; Ganji, D.; Gorji-Bandpy, M.; Soleimani, S. Magnetic field effect on nanofluid flow and heat transfer using KKL model. *J. Taiwan Inst. Chem. Eng.* **2014**, *45*, 795–807. [[CrossRef](#)]
28. Bondareva, N.; Sheremet, M.; Pop, I. Magnetic field effect on the unsteady natural convection in a right-angle trapezoidal cavity filled with a nanofluid: Buongiorno's mathematical model. *Int. J. Numer. Methods Heat Fluid Flow* **2015**, *25*, 1924–1946. [[CrossRef](#)]
29. Hussein, A.K.; Bakier, M.; Hamida, M.B.; Sivasankaran, S. Magnetohydrodynamic natural convection in an inclined T-shaped enclosure for different nanofluids and subjected to a uniform heat source. *Alex. Eng. J.* **2016**, *55*, 2157–2169. [[CrossRef](#)]
30. Yadollahi, A.; Khalesidoost, A.; Kasaeipoor, A.; Hatami, M.; Jing, D. Physical investigation on silver-water nanofluid natural convection for an F-shaped cavity under the magnetic field effects. *Eur. Phys. J. Plus* **2017**, *132*, 372–384. [[CrossRef](#)]
31. Ali, M.; Alim, M.; Akhter, R.; Ahmed, S. MHD natural convection flow of CuO-water nanofluid in a differentially heated hexagonal enclosure with a tilted square block. *Int. J. Appl. Comput. Math.* **2017**, *3*, 1047–1069. [[CrossRef](#)]
32. Purusothaman, A.; Malekshah, E. Lattice Boltzmann modeling of MHD free convection of nanofluid in a V-shaped microelectronic module. *Therm. Sci. Eng. Prog.* **2019**, *10*, 186–197. [[CrossRef](#)]
33. Ghani, I.; Khammas, F.; Mustafa, A.; Hussein, A.K. MHD natural convection in a fully opened parallelogrammic enclosure filled with copper-water nanofluid and partially heated from its left sidewall. *J. Adv. Res. Fluid Mech. Therm. Sci.* **2020**, *74*, 120–145. [[CrossRef](#)]
34. Saha, S. Magnetohydrodynamic buoyancy-driven Al<sub>2</sub>O<sub>3</sub>-water nanofluid flow in a differentially heated trapezoidal enclosure with a cylindrical barrier. *Int. Commun. Heat Mass Transf.* **2020**, *114*, 104593. [[CrossRef](#)]
35. Sourtiji, E.; Hosseinzadeh, S. Heat transfer augmentation of magneto-hydrodynamics natural convection in L-shaped cavities utilizing nanofluids. *Therm. Sci.* **2012**, *16*, 489–501. [[CrossRef](#)]
36. Bakier, M. Flow in open C-shaped cavities: How far does the change in boundaries affect nanofluid? *Eng. Sci. Technol. Int. J.* **2014**, *17*, 116–130. [[CrossRef](#)]
37. Dogonchi, A.S.; Alizadeh, M.; Ganji, D.D. Investigation of MHD Go-water nanofluid flow and heat transfer in a porous channel in the presence of thermal radiation effect. *Adv. Powder Technol.* **2017**, *28*, 1815–1825. [[CrossRef](#)]
38. Alizadeh, M.; Dogonchi, A.S.; Ganji, D.D. Micropolar nanofluid flow and heat transfer between penetrable walls in the presence of thermal radiation and magnetic field. *Case Stud. Therm. Eng.* **2018**, *12*, 319–332. [[CrossRef](#)]
39. Dogonchi, A.; Selimefendigil, F.; Ganji, D.D. Magnetohydrodynamic natural convection of CuO-water nanofluid in complex-shaped enclosure considering various nanoparticle shapes. *Int. J. Numer. Methods Heat Fluid Flow* **2018**, *29*, 1163–1179. [[CrossRef](#)]
40. Rostami, A.K.; Alizadeh, M.; Fazlollahtabar, A.; Ganji, D.D. Performance enhancement of a maple leaf-shaped latent heat energy storage unit by adding nanoparticles and leaf vein fins. *J. Energy Storage* **2021**, *43*, 103159. [[CrossRef](#)]
41. Alizadeh, M.; Nabizadeh, A.; Fazlollahtabar, A.; Ganji, D.D. An optimization study of solidification procedure in a wavy-wall storage unit considering the impacts of NEPCM and curved fin. *Int. Commun. Heat Mass Transf.* **2021**, *124*, 105249. [[CrossRef](#)]
42. Alsabery, A.; Chamkha, A.; Hussain, S.; Saleh, H.; Hashim, I. Heatline visualization of natural convection in a trapezoidal cavity partly filled with nanofluid porous layer and partly with non-Newtonian fluid layer. *Adv. Powder Technol.* **2015**, *26*, 1230–1244. [[CrossRef](#)]
43. Hussein, A.K.; Rout, S.; Fathinia, F.; Chand, R.; Mohammed, H. Natural convection in a triangular top wall enclosure with a solid strip. *J. Eng. Sci. Technol.* **2015**, *10*, 1326–1341.
44. Chand, R.; Rana, G.; Hussein, A. On the onset of thermal instability in a low Prandtl number nanofluid layer in a porous medium. *J. Appl. Fluid Mech.* **2015**, *8*, 265–272.

45. Ahmed, S.; Hussein, A.; El-Aziz, M.A.; Sivasankaran, S. Conjugate natural convection in an inclined square porous enclosure with finite wall thickness and partially heated from its left side wall. *Heat Transf. Res.* **2016**, *47*, 383–402. [[CrossRef](#)]
46. Al-Hafidh, M.H.; Mohammed, H. Natural convection of nanofluid in a cylindrical enclosure filled with porous media. *J. Energy Power Eng.* **2013**, *7*, 2263–2272.
47. Mansour, M.; Ahmed, S.; Bakier, M. Free convection in H-shaped enclosures filled with a porous medium saturated with nanofluids with mounted heaters on the vertical walls. *Spec. Top. Rev. Porous Media-Int. J.* **2013**, *4*, 287–297. [[CrossRef](#)]
48. Baïri, A.; Bauzin, J.; Martin-Garin, A.; Alilat, N.; Millan-Garcia, J. Natural convective cooling of electronics contained in a tilted hemispherical enclosure filled with a porous medium saturated by a water-copper nanofluid. *Int. J. Numer. Methods Heat Fluid Flow* **2019**, *29*, 280–293. [[CrossRef](#)]
49. Raizah, Z.; Ahmed, S.; Aly, A. ISPH simulations of natural convection flow in E-enclosure filled with a nanofluid including homogeneous/heterogeneous porous media and solid particles. *Int. J. Heat Mass Transf.* **2020**, *160*, 120153. [[CrossRef](#)]
50. Molana, M.; Dogonchi, A.; Armaghani, T.; Chamkha, A.; Ganji, D.; Tlili, I. Investigation of hydrothermal behavior of Fe<sub>3</sub>O<sub>4</sub>-H<sub>2</sub>O nanofluid natural convection in a novel shape of porous cavity subjected to magnetic field dependent (MFD) viscosity. *J. Energy Storage* **2020**, *30*, 101395. [[CrossRef](#)]
51. Sheremet, M.; Pop, I.; Rosca, A. The influence of thermal radiation on unsteady free convection in inclined enclosures filled by a nanofluid with sinusoidal boundary conditions. *Int. J. Numer. Methods Heat Fluid Flow* **2018**, *28*, 1738–1753. [[CrossRef](#)]
52. Sheikholeslami, M.; Ganji, D.; Rashidi, M. Ferrofluid flow and heat transfer in a semi-annulus enclosure in the presence of magnetic source considering thermal radiation. *J. Taiwan Inst. Chem. Eng.* **2015**, *47*, 6–17. [[CrossRef](#)]
53. Li, Z.; Hussein, A.K.; Younis, O.; Afrand, M.; Feng, S. Natural convection and entropy generation of a nanofluid around a circular baffle inside an inclined square cavity under thermal radiation and magnetic field effects. *Int. Commun. Heat Mass Transf.* **2020**, *116*, 104650. [[CrossRef](#)]
54. Ul-Haq, R.; Aman, S. Water functionalized CuO nanoparticles filled in a partially heated trapezoidal cavity with inner heated obstacle: FEM approach. *Int. J. Heat Mass Transf.* **2019**, *128*, 401–417. [[CrossRef](#)]